

Spatio-temporal Signatures of Elasto-inertial Turbulence in Viscoelastic Planar Jets

Sami Yamani,^{1,*} Yashasvi Raj,¹ Tamer A. Zaki,² Gareth H. McKinley,¹ and Irmgard Bischofberger^{1,†}

¹*Hatsopoulos Microfluids Laboratory, Department of Mechanical Engineering,
Massachusetts Institute of Technology, Cambridge, Massachusetts 02139, USA*

²*Department of Mechanical Engineering, Johns Hopkins University, Baltimore, Maryland 21218, USA*

(Dated: May 25, 2023)

The interplay between viscoelasticity and inertia in dilute polymer solutions at high deformation rates can result in inertio-elastic instabilities. The nonlinear evolution of these instabilities generates a state of turbulence with significantly different spatio-temporal features compared to Newtonian turbulence, termed elasto-inertial turbulence (EIT). We explore EIT by studying the dynamics of a submerged planar jet of a dilute aqueous polymer solution injected into a quiescent tank of water using a combination of schlieren imaging and laser Doppler velocimetry (LDV). We show how fluid elasticity has a nonmonotonic effect on the jet stability depending on its magnitude, creating two distinct regimes in which elastic effects can either destabilize or stabilize the jet. In agreement with linear stability analyses of viscoelastic jets, an inertio-elastic shear-layer instability emerges near the edge of the jet for small levels of elasticity, independent of bulk undulations in the fluid column. The growth of this disturbance mode destabilizes the flow, resulting in a turbulence transition at lower Reynolds numbers and closer to the nozzle compared to the conditions required for the transition to turbulence in a Newtonian jet. Increasing the fluid elasticity merges the shear-layer instability into a bulk instability of the jet column. In this regime, elastic tensile stresses generated in the shear layer act as an “elastic membrane” that partially stabilizes the flow, retarding the transition to turbulence to higher levels of inertia and greater distances from the nozzle. In the fully turbulent state far from the nozzle, planar viscoelastic jets exhibit unique spatio-temporal features associated with EIT. The time-averaged angle of jet spreading, an Eulerian measure of the degree of entrainment, and the centerline velocity of the jets both evolve self-similarly with distance from the nozzle. The autocovariance of the schlieren images in the fully turbulent region of the jets shows coherent structures that are elongated in the streamwise direction, consistent with the suppression of streamwise vortices by elastic stresses. These coherent structures give a higher spectral energy to small frequency modes in EIT characterized by LDV measurements of the velocity fluctuations at the jet centerline. Finally, our LDV measurements reveal a frequency spectrum characterized by a -3 power-law exponent, different from the well-known $-5/3$ power-law exponent characteristic of Newtonian turbulence.

I. INTRODUCTION

Dilute polymer solutions offer the intriguing engineering opportunity of passively reducing frictional drag in turbulent flows in pipelines [1], in boundary layers around the body of marine vehicles [2], or in open channel irrigation flows [3]. In turbulent pipe flows, the addition of minute quantities of a long chain polymer causes a reduction in the frictional pressure drop per unit length by as much as 40% [4, 5]. The injection of a concentrated polymer solution into the near-wall region of a turbulent boundary layer can reduce skin friction resistance by up to 75%, which can potentially translate into substantial savings in propulsive power requirements and fuel costs [6]. As a consequence of a maximum drag reduction (MDR) asymptote that is independent of polymer concentration, one cannot indefinitely continue to reduce drag by increasing the polymer concentration [7, 8]. While MDR has long been accepted to be an asymptotic limit for drag reduction, it was shown recently that the spatio-temporal dynamics of the flow continue to evolve with increasing polymer concentration [9], and a new state of turbulence driven by viscoelasticity, termed elasto-inertial turbulence (EIT), emerges [10]. EIT encompasses a broad range of Reynolds numbers (Re) [11], characterizing the ratio of inertial forces to viscous forces, and — for an appropriate choice of parameters — drag reduction beyond the MDR limit can be achieved by passing through a relaminarized state [12, 13]. While significant progress has been made in understanding EIT for internal flows, limited work has addressed external flows such as free shear layers. In this work, we investigate inertio-elastic instabilities and turbulence in a canonical geometry commonly used for studying free shear layers; a submerged planar jet of dilute aqueous polymer solution injected into a quiescent tank of water.

* Corresponding author. syamani@mit.edu

† Corresponding author. irmgard@mit.edu

A fully turbulent state develops from the growth of small-amplitude unstable modes and their nonlinear interactions. This turbulent state efficiently mixes the injected polymer solution into the background fluid. The driving mechanisms promoting instability have been investigated through temporal linear stability analysis using the Oldroyd-B model [14] for the planar mixing layer geometry. An increase in the elasticity number (El), characterizing the ratio between the relaxation time scale of the polymer and the vorticity diffusion time scale of the fluid, stabilizes long wavelength instabilities due to an increase in the magnitude of the normal stress differences in the flow [15]. As discussed in E. J. Hinch’s appendix of [15], the stabilizing effect of normal stresses is the result of an effective elastic membrane at the shear layer interface, which generates effects akin to those of surface tension on the Kelvin-Helmholtz instability. It should be noted that this analysis was performed in the dual limit of high Reynolds number and high Weissenberg number (Wi), where Wi characterizes the ratio of the polymer relaxation time scale to the convective time scale of the flow. In this limit, the effects of momentum diffusion, stress relaxation during disturbance growth, and the role of polymer shear stresses are neglected and only the normal stress difference generated by the polymer is considered. A more recent spatio-temporal stability analysis [16] studied the absolute instability of planar shear flow using both the Oldroyd-B and the finitely extensible nonlinear elastic (FENE-P) models [14]. The stabilization of the instability observed in the Oldroyd-B model is shown to be an asymptotic limit that is only valid for large El, while the initial effects of increasing El are, in fact, destabilizing at low and moderate elasticity numbers [16]. Moreover, the local shear rate distribution across the mixing layer plays an important role in determining whether elasticity has a stabilizing or destabilizing effect; only for high enough local shear rates are the normal stress differences large enough to stabilize the flow. A scaled Weissenberg number based on local shear rate and finite extensibility of the polymer chains (L_{max}) was introduced to characterize the stabilizing or destabilizing effect of elasticity, where L_{max} denotes the ratio of the fully extended polymer chain length to the root-mean-square end-to-end separation of the polymer in the equilibrium coiled state. Consistent with the stability analysis, two-dimensional (2D) [17] and three-dimensional (3D) [18] direct numerical simulations of this geometry report that the shear layer is more stable at large elasticity numbers and more unstable to 3D perturbations at small El, compared to a Newtonian shear layer.

In addition to the planar mixing layer, linear stability analyses have been also carried out on more complex flow geometries, including on submerged jets with different velocity profiles. To our knowledge, the earliest analysis on submerged jets is a temporal linear stability analysis on planar and axisymmetric jets with a parabolic velocity profile using the Oldroyd-B model [19], again in the limit of high Reynolds number and high Weissenberg number. It was shown that the bulk fluid column of the jet can become unstable to sinuous or varicose modes of instability, and increasing the elasticity number stabilizes these instabilities through the same mechanism discussed by Hinch in the appendix of [15]. At small elasticity numbers, however, a local shear-layer mode of instability exists close to the edge of the jet with a higher wavenumber compared to the modes that destabilize the jet column. This shear-layer instability is independent of the jet geometry and the jet-column instability. At high elasticity numbers, computations show that this shear-layer mode merges with the jet-column mode [19]. Recent work on the absolute instability of viscoelastic planar jets using a spatio-temporal linear stability analysis [20] introduces a shear layer thickness parameter that allows a more realistic jet velocity profile compared to the parabolic profile considered in [19] as well as a co- or counter-flow parameter allowing for flow in the surrounding fluid reservoir, and uses the FENE-P constitutive model to incorporate the impact of the finite extensibility of the polymer chains. This analysis also finds that increasing the elasticity number can have a destabilizing or stabilizing effect, depending on the velocity profile in the jet.

The nonlinear evolution of instabilities in viscoelastic jets results in EIT, a state of turbulence that is significantly different from Newtonian turbulence. Theoretical [21], computational [22–26], and experimental [27–29] work addressing how the presence of polymers modifies the spatio-temporal features of the turbulent state have suggested a turbulent kinetic energy spectrum that decays with a significantly steeper power-law for elasto-inertial turbulence when compared to the $-5/3$ power-law [30] characterizing Newtonian turbulence. Polymers can temporarily store some of the fluctuating turbulent energy and release it back to the mean flow, inhibiting it from being transferred across the inertial range through the conventional Newtonian turbulent energy cascade [25, 26, 31–33]. The higher wavenumbers of the turbulent spectrum thus have a lower power spectral density (PSD), resulting in a steeper power-law decay in EIT compared to Newtonian turbulence.

In wall-bounded flows, EIT consists of active and hibernating turbulent spots [34–38] generated through transitory energy storage and release by the dissolved polymer chains in the fluid [39]. This energy exchange between macromolecules and the background flow results in alternating vortical and extensional regions [10, 22] that partially or fully suppress the streamwise vortices [10, 40–43]. Computations [44–47] show that one route to EIT is through nonlinearly amplified Tollmien-Schlichting waves that are self-sustained by viscoelasticity. In addition, computations [48–51] and experiments [11] reveal a second route in Poiseuille flow, in which a centerline instability distinguished by arrowhead-shaped coherent structures leads to EIT. This route is similar to that observed for the transition to purely elastic turbulence in the absence of inertia [11, 48–51].

Transition to EIT in free shear layers has so far received relatively limited attention. Viscoelastic jets have been reported to be more stable and to exhibit larger turbulent structures compared to Newtonian jets [52, 53], and the

mean centerline velocity of a round jet follows the same self-similar scaling as a Newtonian jet [54]. Moreover, the viscoelastic jet has a smaller spreading angle and entrains less fluid compared to the Newtonian jet [52, 55–57] due to smaller velocity fluctuations and hence a smaller turbulent kinetic energy (TKE) transfer rate [57]. The turbulent kinetic energy spectrum of the viscoelastic jet calculated from LDV measurements of the velocity fluctuations exhibits a steeper decay compared to that of a Newtonian jet [55, 56]. A quantitative characterization of the role of jet elasticity though has so far been lacking. Direct numerical simulations using the FENE-P model [58] reveal that increasing the Weissenberg number in turbulent viscoelastic jets induces three main differences compared to Newtonian turbulence: (i) Depletion of small-scale vorticity throughout the flow due to the contribution of the polymer chains to vorticity transport, acting as a “counter torque suppressing the generation of vortices” [58], (ii) a tendency for eddy structures to become more elongated due to an increase in extensional viscosity, and (iii) a smaller rate of jet spreading due to the reduction in small-scale vorticity that lowers the viscous dissipation rate [33, 58]. Self-similar solutions were proposed for the rate of jet spreading, the centerline velocity and the maximum polymer stresses using a similarity analysis that is independent of the specific viscoelastic model used for the polymer stress tensor [58]. Through experiments, we have recently identified a universal scaling for the power-law decay of the turbulent kinetic energy spectrum for EIT with an exponent of -3 in viscoelastic axisymmetric jets [29], which corroborates scaling arguments [27, 59] suggesting that in EIT the flexible polymer chains sustain a persistent time-averaged rate of strain and elastic stress through their continuous extension and relaxation.

In this study, we focus on the onset of instability and transition to turbulence in submerged planar jets of dilute aqueous polymer solutions. We experimentally demonstrate the nonmonotonic effect of fluid elasticity on jet stability and characterize the unique spatio-temporal features associated with EIT in the fully-developed turbulent state far from the nozzle. We use laser Doppler velocimetry (LDV) and high-speed schlieren imaging to document the self-similarity of the time-averaged angle of jet spreading and the decay in centerline velocity of the jets with distance from the nozzle, and reveal that the scaling coefficients are independent of fluid elasticity but different from those of a Newtonian jet. We show that EIT generates coherent structures that are larger and more elongated in the streamwise direction compared to Newtonian turbulence. Finally, analysis of the fluctuations in the LDV and schlieren signals measured at the centerline of the jet and in the fully turbulent region far from the nozzle are used to investigate the turbulent kinetic energy spectrum of EIT.

II. EXPERIMENTAL METHODS

A. High-speed stereo-schlieren imaging

A submerged planar jet of water or dilute polymer solution enters a large tank of quiescent water. A planar jet nozzle is generated from a precision glass capillary channel (Vitrocom-2540) with aspect ratio 1:10, where the short side of the capillary channel has an internal dimension $H = 0.4$ mm and the long side has an internal width of $W = 4$ mm, as shown in Fig. 1(a) and (b). We define the hydraulic diameter of the nozzle as $D_h = 2WH/(W + H) = 0.73$ mm. For an ideal planar jet nozzle, in which $W \rightarrow \infty$, and with $H = 0.4$ mm, $D_h \rightarrow 0.8$ mm. The 1:10 aspect ratio capillary channel thus has a hydraulic diameter that is within 10% of the hydraulic diameter of an ideal two-dimensional planar channel. The nozzle exit is placed at depth $\sim 100D_h$ below the air-water interface of the tank.

We use high-speed digital stereo-schlieren imaging to simultaneously visualize the front and side views of the planar jets, as schematically shown in Figure 1(c). We define the coordinate system such that the streamwise direction is in the x -direction and the spanwise directions in the front-view and side-view are in the y - and z -directions, respectively. We define the origin of the coordinate system at the center of the nozzle exit ($x = 0$) such that the exiting fluid stream spans the domain $-H/2 \leq z \leq H/2$ and $-W/2 \leq y \leq W/2$. Schlieren imaging reveals the boundaries of the fine-scale material regions that develop due to the refractive index gradient between the jet and the surrounding fluid as they are advected through the domain in a Lagrangian manner. In each of the two orthogonal schlieren lines shown in Fig. 1(c), the lens closer to the light source collimates the light emitted from the extended LED light source. The collimated light rays are deflected from their original pathway if they pass through a medium with a locally different refractive index compared to the surrounding medium. The lens closer to the camera focuses the light rays on the edge of a knife blade that is adjusted vertically to block a portion of the deflected light rays, resulting in an image of the local light intensity gradient distinguishing the two fluid media (see Supplemental Material for Movies S1-6 [60]).

To understand the capabilities and limitations of our visualization technique, it is helpful to establish criteria for successful schlieren imaging of the evolution of turbulent flow structures in dilute polymer solutions based on optical, fluid, and flow parameters. The sensitivity of a schlieren system is expressed in terms of the minimum detectable

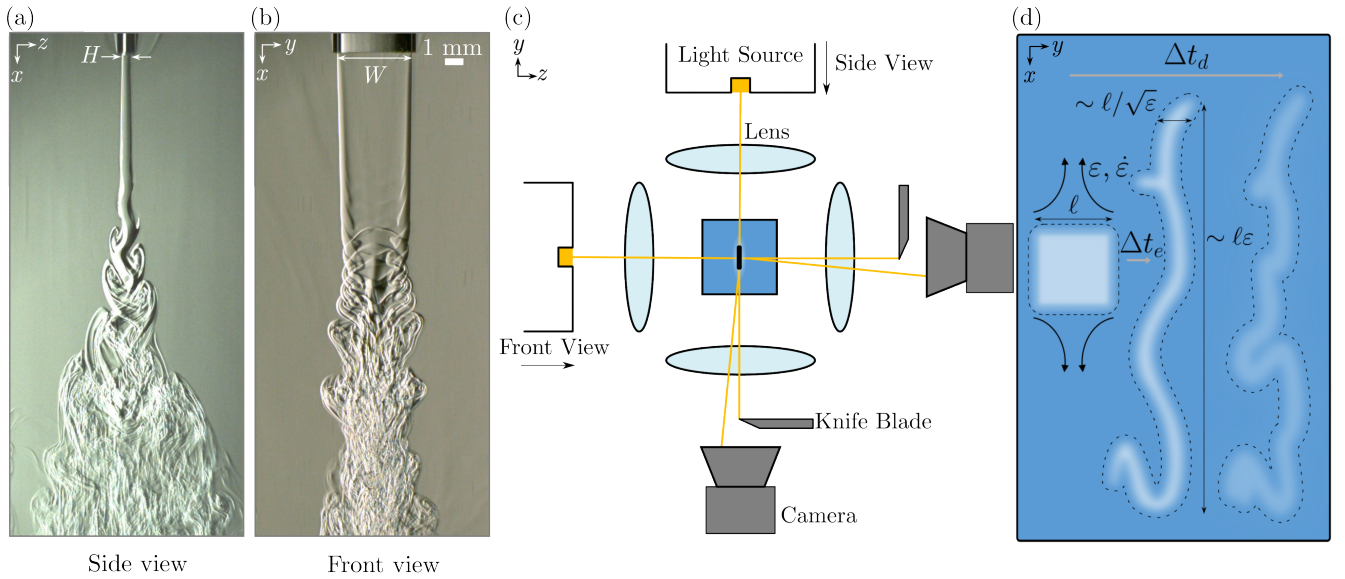


FIG. 1. (a) Side-view and (b) front-view of a turbulent Newtonian jet at $Re = 400$. These views illustrate the jet for the streamwise range of $0 \leq x/D_h \lesssim 50$. (c) Top view schematic diagram of the high-speed stereo-schlieren imaging setup. (d) An illustration of the straining of a material volume of dilute polymer solution with characteristic initial size ℓ (light blue square) in water (dark blue) as a result of a rapid strain ϵ applied at a deformation rate $\dot{\epsilon}$. The time scale for the extension is Δt_e and the time scale for the diffusion of the polymer in the extended material volume due to ϵ is Δt_d . If $\Delta t_e < \Delta t_d$, the evolution of the material volume can be visualized with schlieren imaging, provided that the undeformed material volume has a higher refractive index gradient than the minimum detectable refractive index gradient that sets the sensitivity of the schlieren setup.

refractive index gradient [61],

$$\left(\frac{\partial n}{\partial x_i}\right)_{min} = \left(\frac{\Delta E}{E}\right) \left(\frac{n_0}{L}\right) \left(\frac{a}{f_2}\right), \quad (1)$$

where x_i is the spanwise direction in each schlieren line (y and z for the front-view and side-view schlieren lines, respectively), $\Delta E/E$ is the minimum detectable light contrast (which is $\simeq 2\%$ for our setup), n_0 is the refractive index of the medium ($n_0 = n_{\text{water}} = 1.333$ in our experiments), L is the length scale of the schlieren object being imaged in the direction of the optical axis, $a = 6$ mm is the length of the unblocked part of the light source (which is 10% of the light source width in our experiments), and f_2 is the focal length of the second lens in each schlieren line ($f_2 = 0.3$ m and $f_2 = 0.15$ m for the front- and side-view schlieren lines, respectively). We calculate $\Delta E/E$ for our setup based on the standard deviation of each pixel due to experimental noise. In grayscale (8-bit) imaging, where each pixel has an intensity value between 0 to 255, calibration experiments show that the standard deviation of the pixel intensity when imaging the quiescent bath is ± 6 , thus $\Delta E/E = 6/256 \simeq 0.02$. This yields $(\partial n/\partial y)_{min} = 1.33 \text{ m}^{-1}$ and $(\partial n/\partial z)_{min} = 0.27 \text{ m}^{-1}$ for the front-view and side-view schlieren lines, respectively.

To visualize a static structure with schlieren imaging, the refractive index gradient across the structure should be greater than the value $(\partial n/\partial x_i)_{min}$ for the schlieren setup. For a flow structure of characteristic size ℓ , the refractive index gradient across the structure is denoted $\Delta n/\ell$. For a dilute polymer solution of concentration c , with $\partial n/\partial c$ a material property, we can write $\Delta n/\ell \sim (\partial n/\partial c) \times (c/\ell)$. The ratio of this value to the schlieren sensitivity denotes the static gain of the system. A static structure can thus be successfully visualized with schlieren imaging if the gain is

$$\Gamma_{\text{static}} = \frac{(\partial n/\partial c) (c/\ell)}{(\partial n/\partial y)_{min}} > 1. \quad (2)$$

The static gain can be calculated for the side-view and front-view visualizations using H and W as the characteristic lengths. A 1% wt. water and sucrose solution is used for calibration and for Newtonian jet experiments due to the small density and viscosity difference with water ($< 1\%$) and the known refractive index ($n_{1\% \text{ wt. water-sucrose}} = 1.33445$) [62]. For this solution, $\Delta n/H \simeq 3.63 \text{ m}^{-1}$ and $\Delta n/W \simeq 0.36 \text{ m}^{-1}$, yielding $\Gamma_{\text{static, side}} = 13.60 > 1$ and $\Gamma_{\text{static, front}} = 0.27 < 1$. This is consistent with our visualization shown in Fig. 1(a) and (b). The fluid stream at the nozzle exit can be resolved from the background in the side-view visualization. However, only the lateral edges of the fluid stream at the nozzle

exit ($y \simeq \pm W/2$) are resolved from the background in the front-view visualization and the center of the fluid stream ($y \simeq 0$) has the same light intensity as the background fluid. The static gain criterion determines the size of the largest fluid structures that can be visualized for a particular polymer solution. However, it does not account for the effects of molecular diffusion and cannot predict the size of the finest flow structures that can be visualized with schlieren imaging while they undergo deformations in the flow.

To evaluate the ability to visualize the dynamic evolution of flow structures with schlieren imaging, we consider an arbitrary material volume element of characteristic size ℓ (Fig. 1(d)). A strain rate $\dot{\varepsilon}$ imposed on this material volume element for a time Δt_e leads to a material stretching with true strain $\varepsilon = \dot{\varepsilon}\Delta t_e$. In a uniaxial extension of the material volume (x -direction in Fig. 1(d)) and assuming $\varepsilon \gg 1$, the material volume is extended from an initial length ℓ to a final length $\sim \varepsilon\ell$. Conservation of mass together with incompressibility imply a decrease in the lateral size of this material volume element from ℓ to $\sim \ell/\sqrt{\varepsilon}$ in the orthogonal directions (y - and z -directions in Fig. 1(d)). We seek to understand how this straining affects the distribution and visibility of the polymer solution in the flow. The derivative of the refractive index with respect to the polymer concentration $\partial n/\partial c = (\partial n/\partial y)/(\partial c/\partial y)$ is a material property and constant for a specific polymer solution. It has to remain constant at all times; an increase in $\partial n/\partial y$ results in an increase in $\partial c/\partial y$. An increase in the refractive index gradient, $\partial n/\partial y$, is favorable for visualization as it increases the ratio $(\partial n/\partial y)/(\partial n/\partial y)_{min}$. An increase in the concentration gradient, $\partial c/\partial y$, however, also increases the diffusive flux of the polymer into the background field, which leads to a spreading of the material volume and a progressive homogenization of the polymer concentration. We use Fick's second law to quantify this enhanced diffusive flux,

$$\frac{\partial c}{\partial t} = D \frac{\partial^2 c}{\partial y^2}, \quad (3)$$

where D is the diffusion coefficient of a polymer in a solvent. From Eq. 3, we expect a characteristic diffusion time scale $\Delta t_d \sim \Delta y^2/D$. From Zimm theory [63] the diffusion coefficient is given by

$$D = 0.196 \frac{k_B T}{\eta_s a N^\nu}, \quad (4)$$

where k_B is the Boltzmann constant, T is the temperature, η_s is the solvent viscosity, a is the length of the polymer chain repeat unit ($a = 0.28$ nm for polyethylene oxide (PEO)), N is the number of repeat units in the polymer chain, and ν is the solvent quality parameter ($\nu \simeq 0.6$ for PEO in water). The number of repeat units in a polymer chain scales linearly with the polymer molecular weight ($M_w = 44.05N + 18.02$ for PEO [64]). We thus expect $D \sim N^{-\nu} \sim M_w^{-\nu}$. Using the scaling for D and knowing that $\Delta y \sim \ell/\sqrt{\varepsilon}$, the scaling for the polymer diffusion time scale can be expressed as $\Delta t_d \sim \ell^2/\varepsilon D \sim M_w^\nu$.

The dynamic evolution of a material volume in the flow can be visualized with schlieren imaging only if the enhanced diffusive flux resulting from the steepened concentration gradients in the rapidly stretched material volume is slower than the rate of accumulation in strain. This ratio of time scales is expressed by the Péclet number,

$$\text{Pe} = \frac{\Delta t_d}{\Delta t_e} \sim \frac{(\ell/\sqrt{\varepsilon})^2/D}{\varepsilon/\dot{\varepsilon}} = \frac{\dot{\varepsilon}\ell^2}{\varepsilon^2 D}, \quad (5)$$

which compares the straining time scale of the arbitrary material volume to the enhanced diffusion time scale arising from the large polymer concentration gradients that result from the straining. For $\text{Pe} > O(1)$, the strain of the material element from turbulent velocity fluctuations of strength $\dot{\varepsilon}$ occurs faster than the molecular diffusion. The polymer concentration gradients in the flow thus persist, enabling the evolving Lagrangian material volume to be visualized with schlieren imaging, provided that the imaging speed of the camera is fast enough. This additional criterion expresses a dynamic gain for the schlieren system and acts as a condition for visualizing flow structures of characteristic size ℓ in a rapidly fluctuating flow as they undergo straining deformations of magnitude ε due to strain rates of magnitude $\dot{\varepsilon}$. The dynamic gain can be written as

$$\Gamma_{\text{dynamic}} = \left(\frac{\dot{\varepsilon}\ell^2}{\varepsilon^2 D} \right) > 1. \quad (6)$$

We note that the dynamic gain expressed in Eq. (6) is only a scaling argument for visualization of unstable and turbulent jets since (i) Fick's second law is strictly only valid under no-flow condition and (ii) a jetting flow is not homogeneous uniaxial extension. A material volume element of initial size $\ell \sim D_h = 0.73$ mm that is extended in the x -direction by $\Delta\ell/\ell = \varepsilon \sim 10$ at a Reynolds number of $\text{Re} = 100$ experiences a strain rate of $\dot{\varepsilon} \sim U_0/D_h \sim 100$ 1/s, where U_0 is the mean flow velocity at the nozzle. Considering $D \simeq 10^{-9}$ m²/s for a 1% wt. water-sucrose solution [65], the dynamic gain is $\Gamma_{\text{dynamic}} = \text{Pe} = \Delta t_d/\Delta t_e \sim 1000$. Given that our scaling for the dynamic gain is at least three orders

of magnitude higher than unity, visualization of the evolution of material elements undergoing strong deformations in the flow is possible without the need for additional optical magnification. If the dynamic gain is set to unity, the smallest length scale that can be visualized for these flow conditions, *i.e.* the theoretical resolution, is 2.3×10^{-5} m, which is close to our optical resolution, 2.7×10^{-5} m. The diffusion coefficient of the polymers used in this work is three orders of magnitude smaller than that of water ($D \sim 10^{-12}$ m²/s), which further enhances the dynamic gain. These dynamic gain calculations are consistent with Fig. 1(a) and (b), in which we are able to visualize fine-scale Lagrangian structures in the turbulent flow despite their enhanced diffusion rate.

B. Laser Doppler velocimetry

Schlieren imaging visualizes the evolution of spatio-temporal flow structures in a Lagrangian manner without the need for tracing particles. It is, however, difficult to extract local velocity profiles of the flow and their fluctuations from schlieren images. We use laser Doppler velocimetry (LDV), an Eulerian method that measures the velocity and velocity fluctuations with high temporal resolution at a fixed Eulerian location in the flow.

We use the miniLDV G5B sensor from MSE Inc.. Two laser beams collide at the stand-off distance of the sensor, creating an ellipsoidal probe volume containing multiple interference fringes. The probe volume has a length of 1.5 mm and a diameter of 200 μ m at full width half maximum of the laser intensity profile. The jet is seeded with 10 ppm of Titanium(IV) oxide powder (Sigma-Aldrich, 224227) with grain size smaller than 5 μ m. The particles scatter light as they pass through the bright fringes in the ellipsoidal probe volume. This scattering generates a sinusoidal intensity burst that is detected by a photodetector. The frequency of the Doppler-shifted scattered signal, $f_s(x, z, t)$, at Eulerian location (x, z) and time t , is calculated in real time by applying a bandpass filter and using a fast Fourier transform (FFT) algorithm. Knowing the spacing between fringes, $s = 8.55$ μ m, the instantaneous velocity of the particle is calculated as

$$\tilde{U} = f_s(x, z, t) \times s. \quad (7)$$

The velocity is decomposed into a mean component, $U(x, z)$, and a fluctuating component, $u(x, z, t)$, with zero mean:

$$\tilde{U}(x, y, t) = U(x, z) + u(x, z, t). \quad (8)$$

We align the two beams in the vertical xy -plane at the centerline of the jet ($z = 0$) to measure the streamwise velocity at the centerline of the jet: $\tilde{U}_{cl}(x, t) = U_{cl}(x) + u_{cl}(x, t)$.

The PSD of the velocity fluctuations, also referred to as the turbulent kinetic energy spectrum $E(f)$, provides information about the nature of turbulence. A typical section of a velocity time series is shown in Fig. 2(a) for a Newtonian turbulent jet at $Re = 400$, from which we calculate the PSD shown as a solid line in Fig. 2(b). Additional details on the calculation of the PSD from signals of finite duration are provided in Appendix A.

The measured PSD approaches a plateau at high frequencies that indicates the noise floor inherent to the measurement. The sources of noise include velocity variations within the LDV probe volume, unwanted reflections of the laser beams from surfaces, and the limited sensitivity of the photodetector. The noise level can be subtracted to remove its contribution to the power spectrum, yielding the turbulent kinetic energy power spectrum [28, 66–69]. We follow the approach suggested in Chapter 13 of [70] and fit a power law to the high frequency, noise-dominated region of the spectrum ($f \geq 100$ Hz). This fit can be extrapolated to lower frequencies where the turbulent energy signal is dominant, and is then subtracted across the entire spectrum to access the noise-corrected turbulent kinetic energy power spectrum, as shown by the filled diamonds in Fig. 2(b).

C. Dimensionless numbers and rheological characterization

The dilute polymer solutions studied in this work are formulated from polyethylene oxide (PEO) (Sigma-Aldrich) dissolved in deionized water (Sigma-Aldrich). Five solutions are prepared using PEO with molecular weights $M_w = 4 \times 10^6$ g/mol and $M_w = 8 \times 10^6$ g/mol. The PEO concentration c is kept at $c/c^* < 1$, where c^* is the polymer overlap concentration, to ensure minimal chain-chain interactions. Stock solutions of 0.5% wt. of each molecular weight are gently mixed for at least 10 hours using a roll-mixer to avoid polymer degradation. Samples at different concentrations are prepared by dilution with deionized water. To attain the required refractive index gradient for schlieren imaging, 1% wt. sucrose is added to all solutions. The addition of sucrose changes the viscosity by $\sim 1\%$ and does not affect the elasticity of the solutions.

The dimensionless numbers characterizing the jet are (i) the Reynolds number $Re = \rho U_0 D_h / \eta_0$, where ρ is the fluid

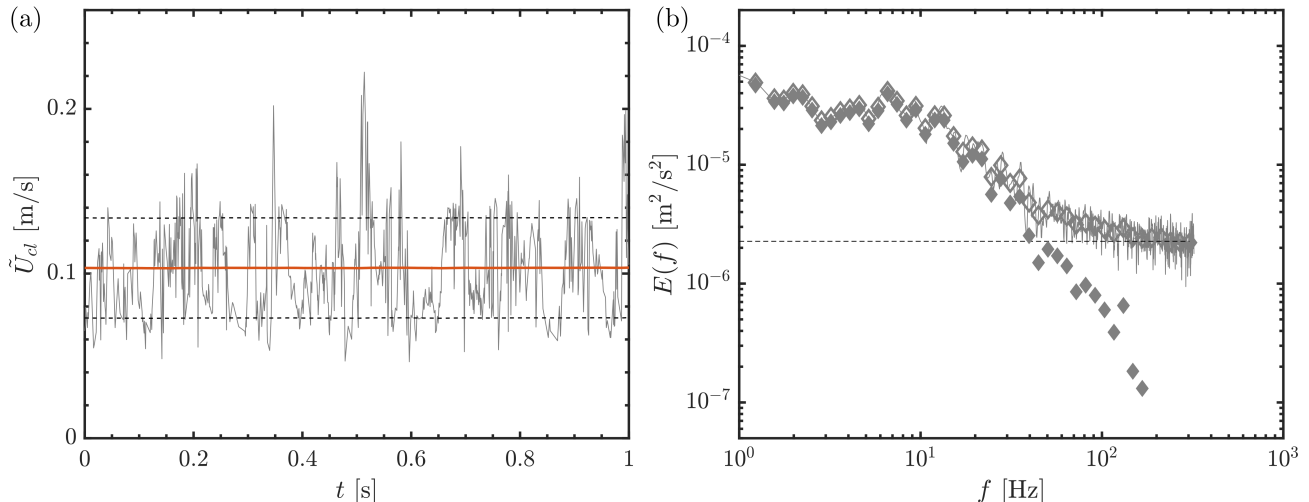


FIG. 2. (a) A section of a velocity time series, $\tilde{U}_{cl}(t)$, at the streamwise location $x = 40D_h$ from the nozzle and at the centerline of the jet for a Newtonian turbulent jet at $Re = 400$. The average data rate is 700 bursts/second. The red solid line denotes the mean centerline velocity, U_{cl} , at $x = 40D_h$, the black dashed lines denote one standard deviation above and below the mean velocity, $U_{cl} \pm u_{cl}^{RMS}$, computed from the entire record of 10,000 bursts collected over 16 seconds. (b) PSD of the velocity fluctuations. The thin solid line denotes the PSD calculated from the LDV velocity measurements. The hollow diamonds (\diamond) denote the PSD averaged over 55 logarithmically spaced bins (~ 22 bins per decade), the dashed line indicates the noise floor of the LDV measurement given by a weak power-law $E_{noise} \sim f^{-0.04}$, and the filled diamonds (\blacklozenge) denote the noise-corrected power spectrum averaged over logarithmically spaced bins.

density, U_0 the mean flow velocity at the nozzle, D_h the hydraulic diameter of the nozzle, and η_0 the zero shear viscosity of the solution, (ii) the elasticity number $El = \eta_p \lambda / \rho (D_h/2)^2$, where $\eta_p = \eta_0 - \eta_s$ is the polymer viscosity and λ the extensional relaxation time, and (iii) the polymer chain extensibility $L_{max} = r_{max} / \langle r_0^2 \rangle^{1/2}$, where $r_{max} \sim M_w$ is the length of a fully extended polymer chain, $\langle r_0^2 \rangle^{1/2} \sim M_w^\nu$ is the equilibrium root-mean-square end-to-end separation of the polymer in the coil state and ν is the solvent quality parameter [63]. From these dimensionless numbers and following previous work on planar jets [58], a Weissenberg number can be defined as $Wi = \lambda U_0 / H \simeq \lambda U_0 / (D_h/2)$. Assuming $D_h \simeq 2H$ due to the large aspect ratio of the nozzle, this yields $El = 2(1 - \beta)(Wi/Re)$, where $\beta = \eta_s / \eta_0$ is the solvent viscosity ratio.

The rheological properties of the solutions are summarized in Table I. The zero shear viscosity η_0 is measured using an Ubbelöhde-type suspended-level capillary viscometer (size 0B, Cannon Instrument) immersed in an isothermal water bath at 25°C. We calculate the reduced viscosity η_{red} as [71, 72]

$$\eta_{red}(c) = \frac{(\eta_0 - \eta_s)}{\eta_s c}, \quad (9)$$

where η_s is the solvent viscosity and c is the polymer concentration. From the Huggins relation [71, 72] we expect

$$\eta_{red} = [\eta] + k_H [\eta]^2 c + O(c^2), \quad (10)$$

where $[\eta]$ is the intrinsic viscosity and k_H the Huggins constant. We extrapolate this linear regression to zero concentration to find the intrinsic viscosity of the polymer in dilute solution. The uncertainty in the intrinsic viscosity increases as the molecular weight of the polymer increases, primarily due to the increase in polydispersity.

Rheological measurements with these dilute polymer solutions indicate that they are weakly shear thinning, as shown in Fig. 3(a), where we report viscosity data for the range of shear rates that the jets experience in the schlieren experiments ($\dot{\gamma} \sim U_0/D_h \leq 1000 \text{ s}^{-1}$). To increase the magnitude of the torque signal, we use a double-wall concentric cylinder geometry on a controlled stress rheometer (DHR3, TA Instruments). Given the weakness of the shear thinning (less than 10% for all samples) we here neglect these effects, following previous experimental studies [10, 12] and report material quantities and dimensionless parameters in terms of zero shear-rate properties. The shear viscosity of our solution was also calculated using the finitely extensible nonlinear elastic-Peterlin (FENE-P) [14] model with the parameters reported in the legend of Fig. 3(a). The predictions are in good agreement with the experimental results for the two solutions with higher polymer concentrations (note the linear scale of the ordinate). The FENE-P model, however, fails to accurately predict the slow and protracted weak shear thinning behavior of the lowest concentration

TABLE I. Composition and material parameters of the polymer solutions at 25°C.

M_w [g/mol]	L_{max}	$[\eta]$ [dl/g]	c^* [ppm]	c [ppm]	c/c^*	η_0 [mPa.s]	λ [ms]	El	β	
4×10^6	68.4	12.1 ± 0.8^a	547 ^b	50	■	0.09	0.98 ± 0.01^c	5 ± 1^d	$(4.0 \pm 1.0) \times 10^{-3}$	0.97
				100	■	0.18	1.04	13 ± 3	$(1.3 \pm 0.3) \times 10^{-2}$	0.88
				200	■	0.37	1.19	21 ± 1	$(4.1 \pm 0.3) \times 10^{-2}$	0.78
				300	■	0.55	1.35	23 ± 0.5	$(6.6 \pm 0.2) \times 10^{-2}$	0.70
8×10^6	91.4	15 ± 5^a	348	150	●	0.43	1.28	54 ± 1	$(1.24 \pm 0.4) \times 10^{-1}$	0.75

* Bold faced values are determined experimentally.

^a Calculated based on zero shear viscosity (η_0) measurements from capillary viscometry. Intrinsic viscosity can also be calculated using the Mark–Houwink–Sakurada equation for PEO, $[\eta] = 0.00072 \times M_w^{0.65}$ [73], which provides 14.08 dl/g and 22.1 dl/g for molecular weights 4×10^6 g/mol and 8×10^6 g/mol, respectively.

^b Calculated using $c^* = 0.77/[\eta]$, where $[\eta]$ is the intrinsic viscosity [73].

^c Measured using Ubbelöhde-type suspended-level capillary viscometer (size 0B, Cannon Instrument) immersed in isothermal water bath at 25°C.

^d Measured using CaBER.

solution. This mismatch potentially arises due to the previously-reported weak aggregation of PEO molecules in ultra-dilute polymer solutions that is slowly disrupted by imposed shear, which cannot be modelled by a simple non-interacting dilute polymer solution model such as the FENE-P dumbbell model [74]. Regardless of this small (less than 1%) quantitative mismatch between experimental and FENE-P model results at the lowest polymer concentration, the small extent of shear thinning predicted by the FENE-P model supports our decision to neglect shear-thinning effects.

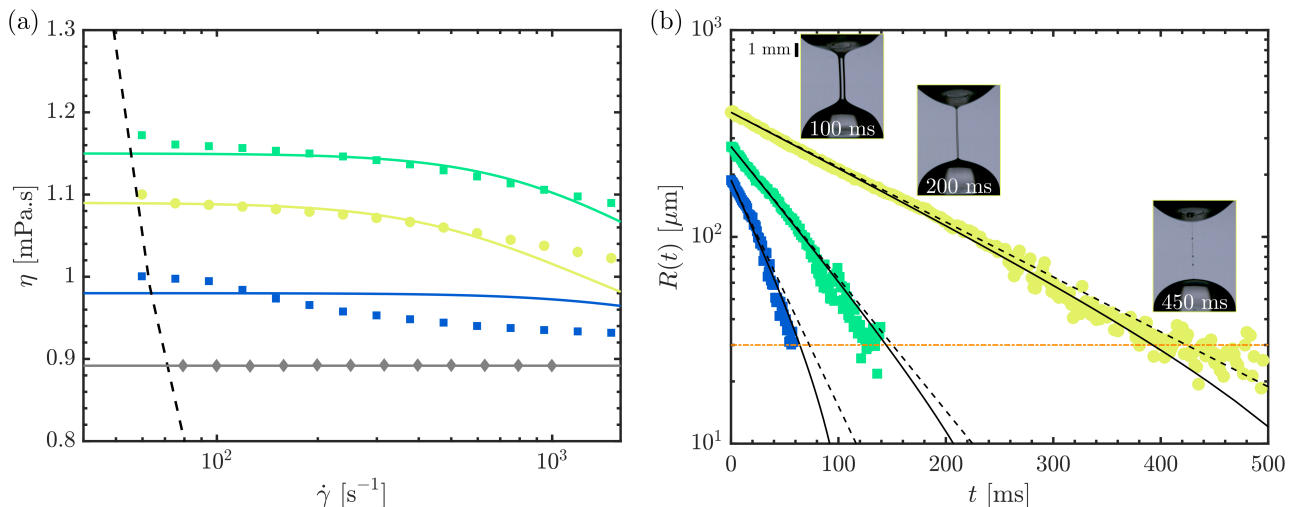


FIG. 3. (a) Shear viscosity of deionized water (\blacklozenge) and the highest concentration PEO solutions used in this work (for which maximum shear thinning is expected), *i.e.*, $El = 0.013$ (\blacksquare), $El = 0.066$ (\blacksquare), and $El = 0.0124$ (\bullet). The solid lines denote the shear viscosity predicted by the FENE-P model for the parameters reported in Table I. The dashed line denotes the low torque limit of the instrument corresponding to $\tau_{min} = 0.1 \mu\text{N.m}$. (b) Evolution of the filament radius at the thinnest axial location, $R(t)$, during filament thinning experiment for the same PEO solutions as in (a). The symbols represent experimental data obtained by image processing of high-speed videos taken in a capillary breakup extensional rheometry (CaBER). Dashed and solid lines correspond to predictions of the Oldroyd-B and FENE-P [14] models, respectively. The dash-dot line denotes the filament radius at which beads-on-a-string structures [75] start to appear. The insets show snapshots of the filament profiles for a PEO solution with $M_w = 8 \times 10^6$ g/mol ($L_{max} = 91.4$) and $c = 300$ ppm.

The extensional relaxation times of the dilute PEO solutions are measured using a capillary breakup extensional rheometer (CaBER) [75]. As the two plates of the CaBER device are separated by a step function, a filament of the viscoelastic test liquid is formed between the plates, which becomes progressively thinner with time under the action of capillary pressure (Fig. 3(b)). A high-speed video is recorded and the evolution of the midpoint radius of the viscoelastic fluid filament with time is measured by an edge-detection algorithm. The extensional relaxation time of the polymer solution is calculated from an elasto-capillary balance on the thinning fluid filament, which becomes appropriate on small length scales [75]. The evolution of the filament radius with time in the elasto-capillary region

is given by

$$\frac{R(t)}{R_0} = \left(\frac{\eta_p R_0}{2\lambda\sigma} \right)^{1/3} \exp\left(-\frac{t}{3\lambda}\right), \quad (11)$$

where $R(t)$ is the midpoint radius of the elastic filament, R_0 is the initial radius of the filament at the start of the elasto-capillary regime, $\eta_p = \eta_0 - \eta_s$ is the polymer contribution to the total viscosity, σ is the surface tension of the polymer solution, and λ is the characteristic extensional relaxation time of the polymer solution [76].

To illustrate how the CaBER results compare with the predictions of the Oldroyd-B and FENE-P models [14], the evolution of the elastic filament radius over time is plotted in Fig. 3(b). We follow the derivation in [77] for the evolution equation of the filament radius with time based on the Oldroyd-B and FENE-P models in the elastocapillary regime (see Appendix B for details). The critical radius below which the ligament is no longer a uniform elastic thread but develops a beads-on-a-string morphology [76] is shown with a horizontal dash-dot line. It should be noted that while the kinematics of a planar jet are shear dominated, it is far from steady simple shear or uniaxial extension that are used here to characterize the rheological properties of the solutions. Rheological characterization under conditions of homogeneous prescribed deformation, however, is indispensable for reproducing our jet experiments or for performing complementary numerical simulations and data assimilation [78–80].

To calculate the polymer chain extensibility $L_{max} = r_{max}/\langle r_0^2 \rangle^{1/2}$, the length of a fully extended polymer chain, r_{max} , is estimated using $r_{max} = lM_w/m_0$, where $l = 0.28$ nm is the length and $m_0 = 44$ g/mol the molar mass of the ethylene oxide repeat unit [81]. The equilibrium root-mean-square end-to-end separation of the polymer in the coil state is $\langle r_0^2 \rangle^{1/2} = \sqrt{6}R_g \sim M_w^\nu$, where ν is the solvent quality parameter, and R_g is the equilibrium radius of gyration of the polymer in the coil state [82].

III. RESULTS AND DISCUSSION

A. Stability of Newtonian and viscoelastic planar jets

As the Reynolds number increases, our high-speed schlieren images show that the unperturbed jets transition from a laminar state to an unsteady state and ultimately to a fully turbulent state, as shown in Supplemental Material, Movies S1-S6 [60] and Appendix C. At a Reynolds number $Re = 100$, the jets show the evolution and growth of disturbances but have not yet transitioned to a turbulent state over the field of view ($x \leq 50D_h$). An increase in the elasticity number first makes the planar jet more unstable, but then subsequently partially stabilizes the jet at higher elasticity numbers, as seen in the front-view schlieren snapshots in Fig. 4 and in the Supplemental Material, Movie S7 [60]. To quantify these observations we use dynamic mode decomposition (DMD) [83].

DMD decomposes the disturbances into a linearized set of harmonic contributions and identifies the dominant unstable modes. It is a singular value decomposition-based method that can be performed both temporally and spatially [84]. To perform spatial DMD in the streamwise direction (x -direction), we represent the region of interrogation indicated by the dashed white lines in Fig. 4 as a digital intensity signal $I(x, y, t)$. The intensity signal from the high-speed schlieren images can be written as a linear sum of orthogonal modes $\phi(y, t)$, each having a complex amplitude b , and a complex wavenumber $k = k_r + ik_i$:

$$I(x, y, t) = \sum_{j=1}^{N_x} b_j \phi_j(y, t) \exp(k_r^j + ik_i^j)x, \quad (12)$$

where $j = 1, 2, \dots, N_x$ and N_x is the total number of decomposed modes. The magnitude $|b_j|$ determines the relative importance of each mode compared to others, k_i^j is the wavenumber characterizing the periodicity of the mode in the streamwise x -direction and k_r^j is the growth rate of the mode where $k_r^j > 0$ represents a spatially growing mode.

The maximum number of resolvable modes is proportional to the length of the data series in space or time (depending on whether spatial or temporal DMD is performed) [83]. Retaining all the modes derived from intrinsically noisy experimental data, however, is unwieldy as a large number of relatively weak modes over a wide range of wave numbers or frequencies with approximately equal weighting are observed. To avoid this issue, we identify the optimal number of modes, N_x^* , at which the mean squared error between the modal representation and the original schlieren signal exhibits an “elbow” corresponding to a distinct change in slope [84]. To determine the elbow point, we adopt two linear fits, one to the points with mean squared error higher than the estimated N_x^* and one to the points with lower mean square errors. We adjust the estimate of N_x^* until it minimizes the sum of errors of the two fits. To ensure the robustness of the modes identified by DMD, we also spatially extend the DMD region of interrogation as explained in

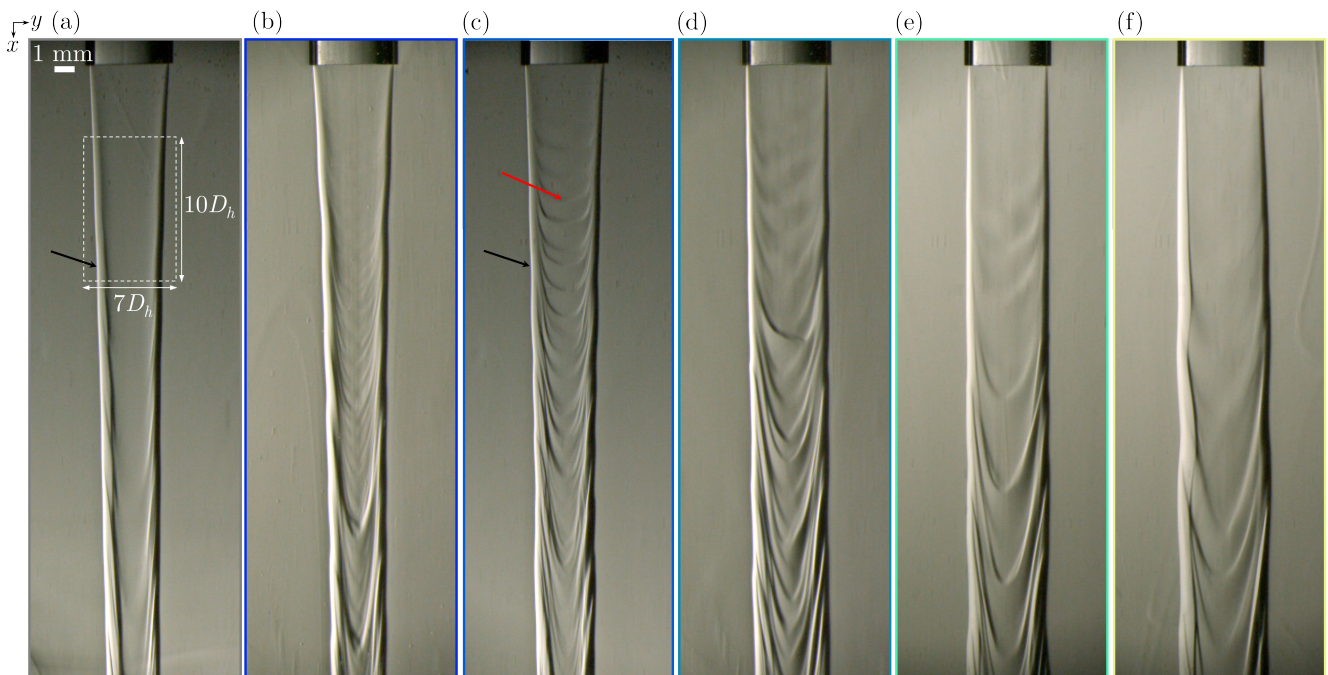


FIG. 4. Front-view schlieren snapshots of jets at $Re = 100$: (a) Newtonian jet ($El = 0$), (b) $El = 0.004$, (c) $El = 0.013$, (d) $El = 0.041$, (e) $El = 0.066$, and (f) $El = 0.124$. The elasticity number and hence the Weissenberg number $Wi \sim El \cdot Re / (1 - \beta)$ increases from left to right. The dashed rectangle indicates the region of interrogation used for the DMD analysis. The black arrows denote the the jet column modes, the red arrow denotes the shear layer modes.

Appendix D. The same primary modes are identified for different regions of interrogation, however, DMD identifies additional slower growing modes when applied on a larger region of interrogation.

A temporal DMD analysis (reported in Appendix D) shows that the jets are stable in time, indicating that the instabilities are not absolute in nature. A spatial DMD analysis reveals a number of unstable modes indicating the *convective* nature of the instability, as shown in Fig. 5 and 6. Each orthogonal mode ϕ_j is characterized by three parameters: the wavenumber k_i^j , the growth/decay rate k_r^j , and the amplitude $|b_j|$. The wavenumber and growth rate of the modes identified for a Newtonian jet and a viscoelastic jet with $El = 0.013$ are shown in Fig. 5. Here, filled symbols denote spatially growing modes with $k_r > 0$, hollow symbols denote spatially decaying modes with $k_r < 0$, and the symbol size denotes the relative magnitude of the modal amplitude with respect to the DC mode. The modal amplitude determines the relative contribution of that mode to the reconstruction of the original schlieren image; the larger the amplitude the greater the modal contribution. Both the Newtonian and the viscoelastic jet have a dominant unstable mode at a low wavenumber $k_i D_h \simeq 1.3$, while the viscoelastic jet has an additional dominant unstable mode at a higher wavenumber $k_i D_h \simeq 3.7$, as shown in Fig. 5. The dominant low wavenumber modes of each jet (Fig. 5(c) and (d)) denote periodicity at the lateral edges ($y \simeq \pm W/2$) of the jet that results in bulk undulations in the entire jet column. We refer to these modes as “jet-column” modes. The additional strong orthogonal mode present in the viscoelastic jet at higher wavenumbers, by contrast, denotes spanwise undulations (clearly observable in Fig. 5(e)) that are persistent near the center of the jet ($y \sim 0$), which result in a shear-layer instability at the interface between the fast-moving jet and the quiescent background fluid ($z \simeq \pm H/2$). We refer to these modes as “shear-layer” modes. To further clarify the difference between jet-column and shear-layer modes, we show side- and front-view snapshots of the Newtonian and viscoelastic jets at $Re = 150$ in Fig. 5(f)-(i). The Newtonian jet (Fig. 5(f) and (g)) shows a sinuous jet-column mode, but no shear-layer mode of instability. The viscoelastic jet (Fig. 5(h) and (g)) similarly shows a sinuous jet-column mode of instability and, additionally, an independent shear-layer instability that grows near the interface between the jet and the background fluid ($z \simeq \pm H/2$ and $-5H \lesssim y \lesssim 5H$, marked with red circles in Fig. 5(h) and (i)).

In Fig. 6, we explore the evolution of the dominant shear-layer mode with elasticity number for the jets shown in Fig. 4. As the elasticity number increases, the wavenumber associated with the shear-layer mode decreases, while the wavenumber associated with the jet-column mode remains almost unchanged. For $El = 0.124$, we are unable to distinguish two distinct modes of instability and only a single dominant mode is identified. This is consistent with Rallison & Hinch’s argument that the jet-column and shear-layer modes merge at higher elasticity numbers [19]. These findings allow us to rationalize the observations in Fig. 4; the emergence of the viscoelastic shear-layer instability

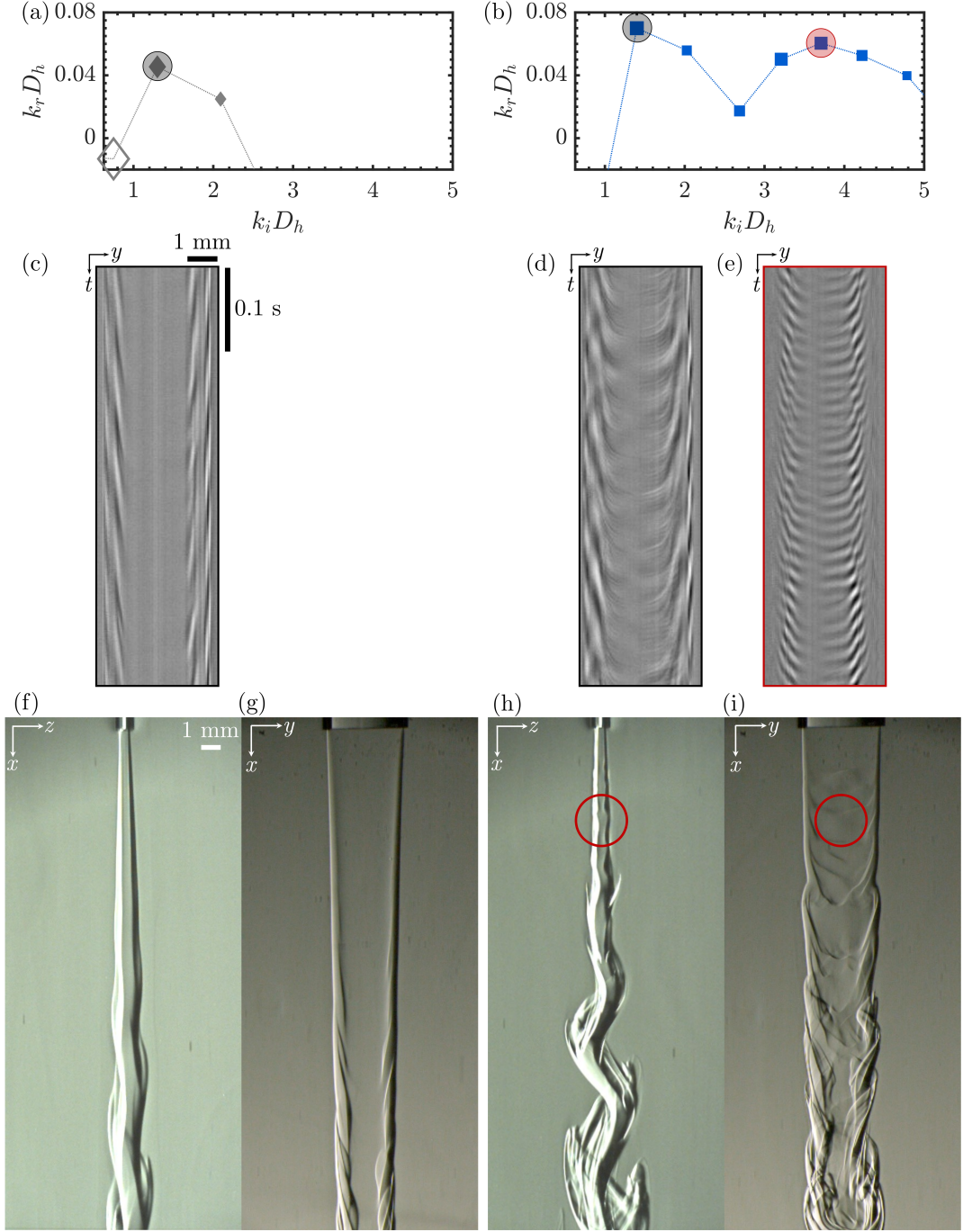


FIG. 5. Wavenumber and growth rate of orthogonal modes determined using DMD for (a) a Newtonian and (b) a viscoelastic ($El = 0.013$) jet at $Re = 100$. The abscissa starts from the smallest wavenumber that we can resolve, set by our region of interrogation. The size of the symbols denotes the relative magnitude of the modal amplitude $|b_j|$ with respect to the DC mode. Filled and hollow symbols denote unstable and stable modes, respectively. The dashed lines are guides to the eye for identifying the local maxima in disturbance growth rate. The dominant jet-column and shear-layer modes are marked with gray and red shaded circles, respectively. (c) The spatio-temporal structure of the orthogonal mode associated with the dominant unstable wavenumber in the Newtonian jet (indicated by the gray circle in (a)). (d) The spatio-temporal structure of the orthogonal mode associated with the dominant unstable low wavenumber in the viscoelastic jet (marked with a gray circle in (b)). (e) The spatio-temporal structure of the orthogonal mode associated with the dominant unstable high wavenumber in the viscoelastic jet (marked with a red circle in (b)). (f, g) Snapshots of the Newtonian jet at $Re = 150$. A long wavelength (small wavenumber) sinuous jet-column mode is visible, but no shear-layer mode is identifiable. (h, i) Snapshots of the viscoelastic jet with $El = 0.013$ at $Re = 150$. Both a low wavenumber sinuous jet-column mode and a high wavenumber shear-layer mode are detected. The shear-layer mode is marked with a red circle.

destabilizes the jet, whereas its subsequent merging with the jet-column mode partially re-stabilizes the jet, accounting for the competing effects of increasing elasticity number on jet stability. Our results are, to our knowledge, the first experimental manifestation of the shear-layer and jet-column modes in viscoelastic jets that were previously identified in a temporal linear stability analysis [19]. The shear-layer mode present for small non-zero elasticity numbers within the shear layer at the edge of the jet is independent of the jet geometry and velocity profile and orthogonal to the longer wave jet-column instability modes. In this low El regime, the effects of elasticity are important only within a thin sheared layer close to the jet edge where the fluid inertia is smaller (compared to the core of the jet), but where the shear rate is higher compared to the core of the jet, resulting in a large first normal stress difference. Rallison & Hinch argue that the interplay between inertial and elastic effects results in a low pressure region just outside the jet and a crowding of the streamlines. Such crowding induces a dilation of the streamlines just inside the jet in the thin edge region where elasticity dominates. The crowding and dilation of the streamlines generates the local shear-layer instability. Their calculations show that the wavenumber associated with the local shear-layer instability decreases with an increase in elasticity number [19], which is supported by our experimental findings. The confinement of the shear-layer mode of instability to the very edge of the jet ($z = \pm H/2$) implies that it can occur for both planar and

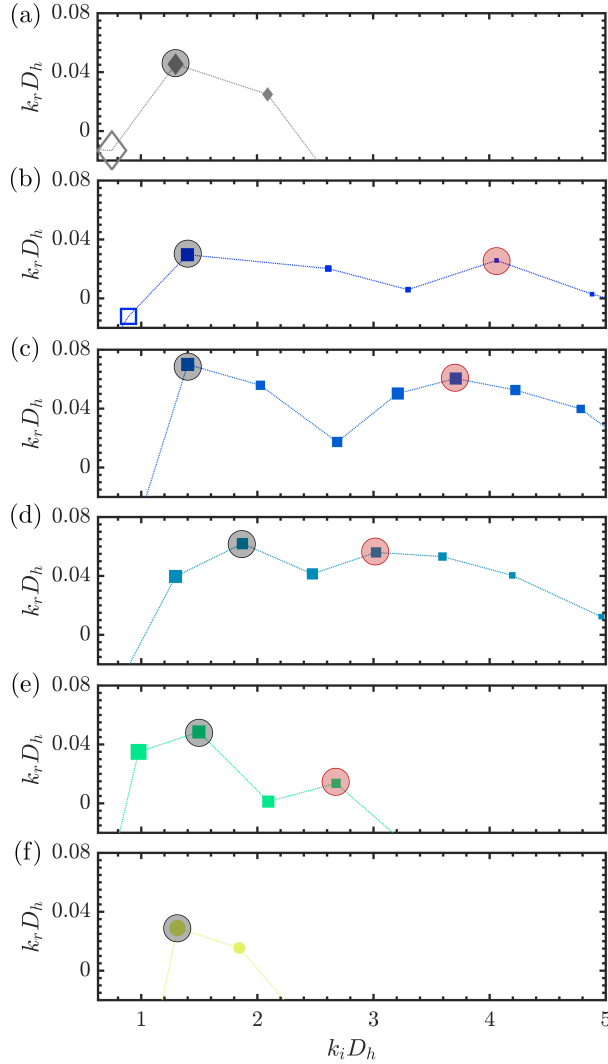


FIG. 6. Wavenumber and growth rate of orthogonal modes for (a) Newtonian (\blacklozenge), (b) El = 0.004 (\blacksquare), (c) El = 0.013 (\blacksquare), (d) El = 0.0041 (\blacksquare), (e) El = 0.066 (\blacksquare), and (f) El = 0.124 (\bullet) jets at Re = 100. The abscissa and ordinate are nondimensionalized with the jet hydraulic diameter D_h . The abscissa starts from the smallest wavenumber that we can resolve based on our region of interrogation. The size of the symbols denotes the relative magnitude of the modal amplitude $|b_j|$. Filled and hollow symbols denote unstable and stable modes, respectively. The jet-column and shear-layer modes with highest growth rate are marked with shaded gray and red circles, respectively. The dashed lines are guides to the eye for identifying the local maxima in growth rate.

axisymmetric jets, irrespective of whether the fluid jet column is unstable to a sinuous or a varicose mode. As the elasticity number increases, the thickness of the sheared fluid layer in which elastic effects are dominant increases, which eventually results in the merging of the shear-layer instability and the jet-column instability [19]. While the shear-layer instability identified in this study is an inertio-elastic instability that is limited to the viscoelastic jets, a Newtonian jet can also undergo an inertial shear-layer instability but typically at much higher Reynolds numbers ($\text{Re} \geq 8000$) [85]. For the range of Reynolds numbers investigated, we do not observe an inertial and spatially growing shear-layer instability in the Newtonian jet.

The jet instabilities demonstrated here lead ultimately to the transition to turbulence. The emergence of the spatially growing viscoelastic shear-layer mode at small, but finite, elasticity numbers induces a transition to turbulence at a lower Reynolds number compared to the Newtonian jet, as shown in Appendix C. At a fixed Reynolds number, the jets for which a viscoelastic shear-layer mode emerges show a transition to turbulence at a streamwise Eulerian location that is closer to the nozzle compared to the Newtonian jet. The merging of the shear-layer mode with the jet-column mode at higher elasticity numbers results in a delay in transition to turbulence until higher Reynolds number (compared to the low elasticity number jets). Similarly, at a fixed Reynolds number, our schlieren imaging shows that the high elasticity number jets transition to turbulence at streamwise Eulerian locations that are further from the nozzle compared to the low elasticity number jets. This effect is explored and quantitatively studied for turbulent planar jets in the next section.

B. Self-similarity of planar jets

The nonlinear evolution of the shear-layer and jet-column instability modes results in the transition of the viscoelastic jets to an EIT state. In this state, the jets spread laterally, and the spreading is a measure of the jet entrainment process. To quantify this lateral spreading, we calculate the standard deviation of the time-varying intensity for each pixel in the side-view schlieren images over the duration of the experiment, as shown in the inset of Fig. 7(a). We employ Otsu's method [86–88] to detect the lateral boundary of the region affected by turbulent fluctuations. Following [58, 89], we define the jet spreading parameter δ as the distance from the centerline of the jet to the boundary, as reported in Fig. 7(a) for jets at $\text{Re} = 400$. For both Newtonian and viscoelastic jets, we find the jet spreading can be written in the form $\delta/D_h = A_\delta (x - x_0)/D_h$, where A_δ is the coefficient of spreading and x_0 denotes the extrapolated or virtual origin of the turbulent jet. While the $\delta \sim x$ scaling is consistent with the self-similarity analysis [58], such a scaling analysis does not provide values for A_δ and x_0 and experiments or numerical simulations are required to obtain them. For the Newtonian jet we find a coefficient of spreading that is larger than the typical values reported in the literature at Reynolds numbers that are higher than our investigated Reynolds number [90]. Our results are in qualitative agreement with [91], a study at Reynolds numbers comparable to ours. A quantitative comparison of A_δ , however, is challenging as our calculation method for δ is different from that used in [91]. Our experiments show that all viscoelastic jets transition to turbulence at an Eulerian position that is closer to the nozzle compared to the Newtonian jet resulting in dramatically reduced values of the virtual origin x_0 , as shown in Fig. 7(b). For small, non-zero elasticity numbers ($0.004 \lesssim \text{El} \lesssim 0.04$), the transition to turbulence occurs at a streamwise location very close to the nozzle, consistent with the emergence of the shear-layer instability in these jets. A further increase in elasticity number to values where the shear-layer mode merges with the jet-column mode ($\text{El} \gtrsim 0.04$) results in a moderate increase in x_0/D_h , as shown in Fig. 7(b). The coefficient of spreading is smaller for viscoelastic jets compared to the Newtonian jet, but is unchanged within our experimental resolution for a range of elasticity numbers $0.004 < \text{El} < 0.124$, indicating that viscoelastic jets in the EIT state maintain a universal entrainment rate.

Furthermore, we measure the mean centerline velocity U_{cl} for the Newtonian and viscoelastic ($\text{El} = 0.013$) jets at fixed Eulerian positions on the centerline of the jet and in the streamwise direction using LDV. The center of the probe volume is aligned with the centerline of the jet, and the probe volume is smaller than the smallest lateral dimension of the jet enabling good resolution of the centerline velocity. The velocity profile of both jets follows $U_{cl} \sim x^{-1/2}$, which suggests that the velocity profile in the turbulent region of the jets can be written in the similarity form $(U_{cl}/U_0)^{-2} = A_U (x - x_0)/D_h$ [58], as shown in Fig. 7(d), where A_U is the similarity coefficient for the velocity profile. For the Newtonian jet, the velocity similarity coefficient matches the value reported in an earlier study [91] at the same Reynolds number. The viscoelastic jet has a smaller similarity coefficient, A_U , compared to its Newtonian counterpart, which is consistent with its smaller coefficient of spreading, A_δ . The smaller rate of spreading of the viscoelastic jet results in a lower rate of entrainment and a smaller rate of vorticity diffusion. From conservation of mass, this implies that the rate of decay of the centerline velocity is slower than that of the Newtonian jet.

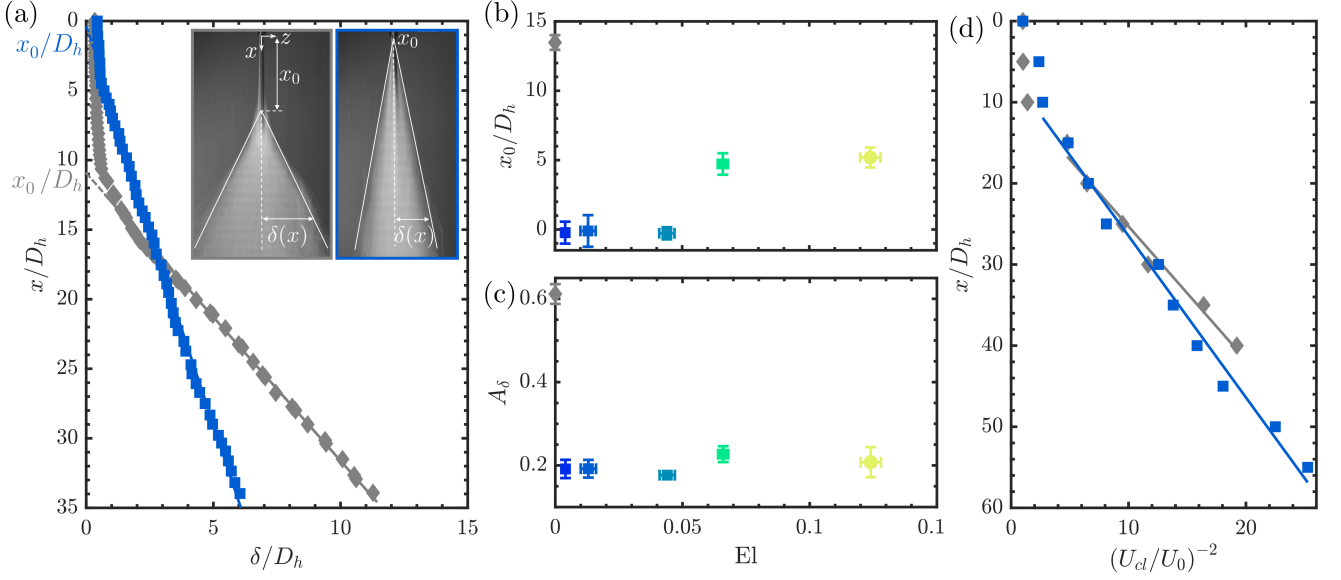


FIG. 7. (a) Turbulent spreading of a Newtonian jet (\blacklozenge) and a viscoelastic jet with $El = 0.013$ (\blacksquare) calculated from the standard deviation of intensity fluctuations in side-view schlieren images, shown in the inset, at $Re = 400$. To enable identification of the nozzle location and the laminar region of the jets in the insets, the standard deviation images are overlaid on the image of the mean of each pixel over the duration of the experiment. The lateral spreading of the jets at dimensionless streamwise locations x/D_h is denoted by δ . The onset of the self-similar turbulent region correspond to a virtual origin x_0 . The symbols denote the profile extracted from the images, the solid lines denote a linear fit to the turbulent region. The relationships between the jet spreading and the streamwise distance from the nozzle in the turbulent region are $\delta/D_h = (0.61 \pm 0.02)(x - x_0)/D_h$ and $\delta/D_h = (0.19 \pm 0.02)(x - x_0)/D_h$ for the Newtonian and viscoelastic jets, respectively. (b) The extrapolated origin x_0 of turbulent jets as a function of elasticity number El at $Re = 400$. (c) Coefficient of spreading A_δ versus elasticity number at $Re = 400$. (d) The normalized streamwise mean centerline velocity, U_{cl}/U_0 , for a Newtonian and a viscoelastic ($El = 0.013$) jet scales as $U_{cl}/U_0 \sim (x/D_h)^{-1/2}$, where U_0 is the mean velocity at the nozzle exit. The relationships between the normalized velocity and the streamwise distance from the nozzle in the turbulent region are $(U_{cl}/U_0)^{-2} = (0.60 \pm 0.06)(x - x_0)/D_h$ and $(U_{cl}/U_0)^{-2} = (0.50 \pm 0.04)(x - x_0)/D_h$ for the Newtonian and viscoelastic jets, respectively.

C. Lagrangian coherent structures in elasto-inertial turbulence of planar jets

The concept of Lagrangian coherent structures can be extended from Newtonian turbulence to elasto-inertial turbulence to understand how viscoelasticity affects the evolution of material regions in a time-dependent turbulent flow [51]. Coherent structures are local material regions of the flow whose dynamics contain a significant portion of the total energy in the flow and that remain correlated over sufficiently large spatio-temporal scales [51]. Common experimental techniques such as LDV or particle image velocimetry must be coupled with advanced non-linear dynamics data processing techniques such as the Finite Time Lyapunov Exponent [92] or Diffusion Barrier Strength approach [93] to determine the spatio-temporal evolution of material regions. Schlieren imaging directly reveals the Lagrangian evolution in the boundaries of the fine-scale material regions as they are advected through the domain.

Our schlieren images provide unique visualization of the characteristic features in fully-developed elasto-inertial turbulence and Newtonian turbulence in planar jets, as shown in Fig. 8(a)-(d) and Supplemental Material, Movie S8 [60] for $Re = 400$. Similar to the behavior observed at lower Reynolds numbers, increasing the elasticity number first has a strongly destabilizing effect and makes the jet turbulent at a streamwise location closer to the nozzle, while a further increase in elasticity number moves the onset of the turbulent region further downstream due to merging of shear-layer and jet-column modes, as shown in Fig. 8(a)-(d). The shear-layer modes create streamwise aligned coherent structures that are an elasto-inertial analog reminiscent of Emmons turbulent spots [94–96], marked with red circles in Fig. 8(b)-(d). The absence of shear-layer modes in the Newtonian jet prevents observation of these local turbulent patches, where the jet transitions to turbulence before turbulent spots can form due to the braiding and roll-up of vortices arising from the nonlinear evolution of the jet-column modes.

To identify the key features of these Lagrangian coherent structures (LCSs), we select a square region of interrogation in the front-view schlieren images of size $4D_h \times 4D_h$, with its centroid located at the streamwise distance of $x = 40D_h$ from the nozzle. We evaluate the size and orientation of the turbulent structures by calculating the two-dimensional (2D) autocovariance for the region of interrogation for each jet at a fixed value of $Re = 400$, as shown in Fig. 8(e)-(h).

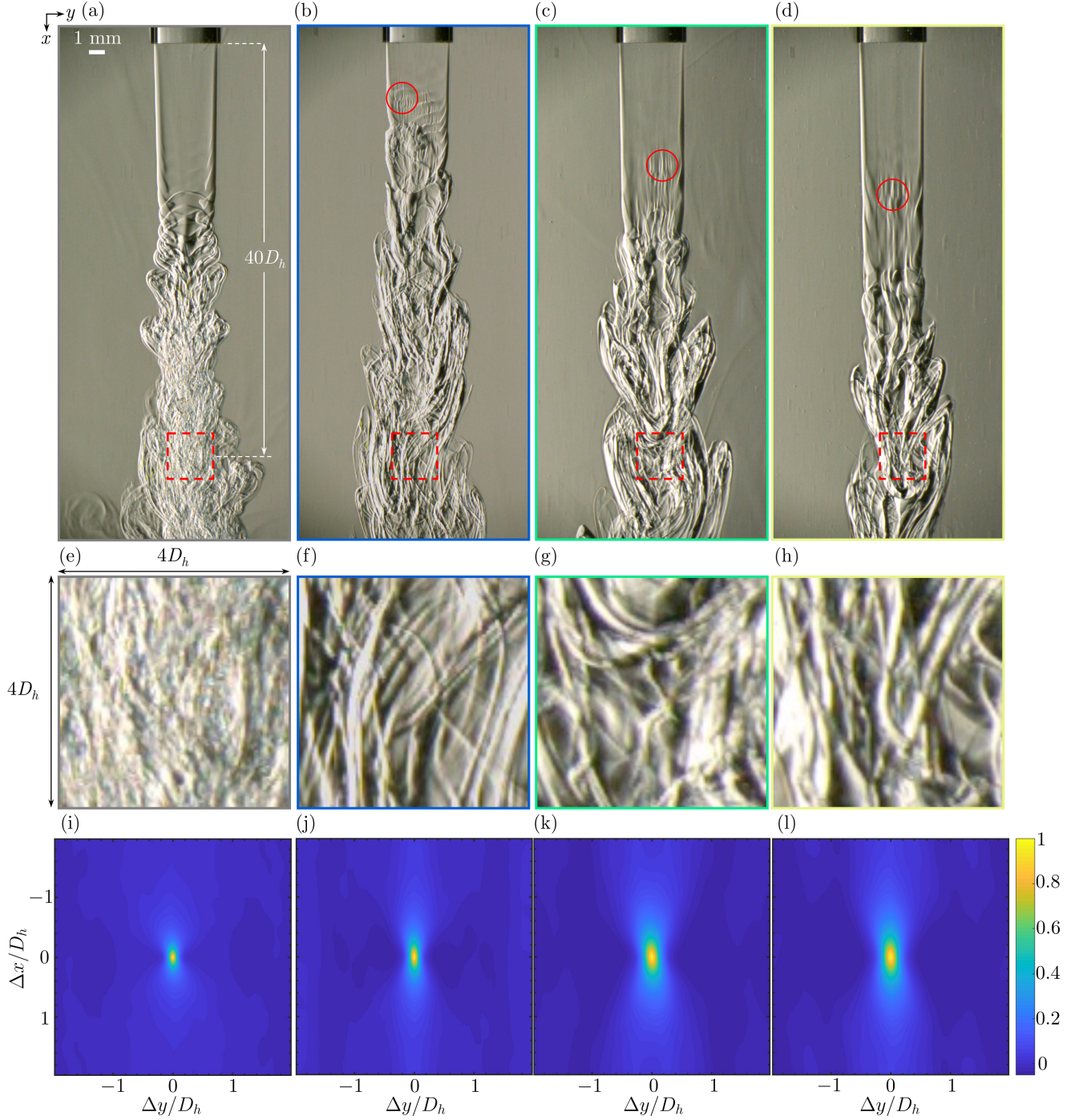


FIG. 8. Front-view schlieren snapshots of (a) a Newtonian jet and (b-d) viscoelastic jets with (b) $El = 0.013$ (c) $El = 0.066$, and (d) $El = 0.124$ at $Re = 400$. The regions of interrogation of size $4D_h$ are indicated by the red squares. (e-f) Magnified regions of interrogation for the jets shown in (a-d), highlighting how an increase in elasticity number modifies the structure of turbulence. (i-l) Two dimensional auto-covariance of the regions of interrogation shown in (e-f). The color bar indicates the average value of the 2D autocovariance \bar{R} .

The autocovariance is first calculated for each schlieren snapshot,

$$R(\Delta x, \Delta y, t) = \frac{\sum_{x,y} (I(x, y, t) - \bar{I}) (I(x + \Delta x, y + \Delta y, t) - \bar{I})}{\left[\sum_{x,y} (I(x, y, t) - \bar{I})^2 \sum_{x,y} (I(x + \Delta x, y + \Delta y, t) - \bar{I})^2 \right]^{1/2}}, \quad (13)$$

where $I(x, y, t)$ is the intensity of the schlieren image at position (x, y) and at time t , and \bar{I} is the average intensity of the region of interrogation over space and time. The average value of the 2D autocovariance is then calculated by computing the expectation over all snapshots, $\bar{R}(\Delta x, \Delta y) = \mathbf{E}[R(\Delta x, \Delta y, t)]$. The contours of \bar{R} are shown in Fig. 8(i)-(l), where the color bar denotes autocovariance values of $-0.05 < \bar{R} < 1$ from dark blue to yellow. Increasing elasticity number increases \bar{R} in the streamwise direction, x , as shown in Fig. 9(a) and (b), where we report the streamwise and spanwise values of the autocovariance, \bar{R}_{xx} and \bar{R}_{yy} , (see inset of Fig. 9(b) for definition) as a function of nondimensionalized streamwise and spanwise displacements, $\Delta x/D_h$ and $\Delta y/D_h$, respectively. The streamwise correlation decays more slowly than the spanwise correlation for all jets, due to the non-zero mean shear in the flow. In addition, the viscoelastic jets have a higher streamwise correlation than the Newtonian jet for all values of El. The rate of decay in the spanwise correlation, however, remains similar for Newtonian and viscoelastic jets. Elasto-inertial turbulence is thus characterized by coherent structures in the form of material regions that are more elongated in the streamwise direction compared to those observed in Newtonian turbulence. This is further confirmed by a polar representation of the 2D autocovariance, as shown in Fig. 9(c) for a radial displacement $\Delta r = 0.25D_h$. In this representation, $\theta = 0$ and $\theta = \pm\pi/2$ represent \bar{R}_{xx} and \bar{R}_{yy} , respectively. The variations with elasticity number in the values of streamwise and spanwise correlations at $\Delta x/D_h = \Delta y/D_h = 0.25D_h$ are summarized in Fig. 9(d). The viscoelastic jets have a streamwise correlation value that is statistically higher than that of the Newtonian jet for all elasticity numbers, while the spanwise correlations of the jets do not show a statistically significant difference. The observation that the streamwise and spanwise correlations are independent of elasticity number for the viscoelastic jets further supports the universality of EIT [29]. The schlieren observations of elongated and flow-aligned material domains are consistent with the suppression of streamwise vortices by EIT that has previously been reported in numerical simulations of turbulent wall-bounded shear flows [10, 22, 35, 40, 41].

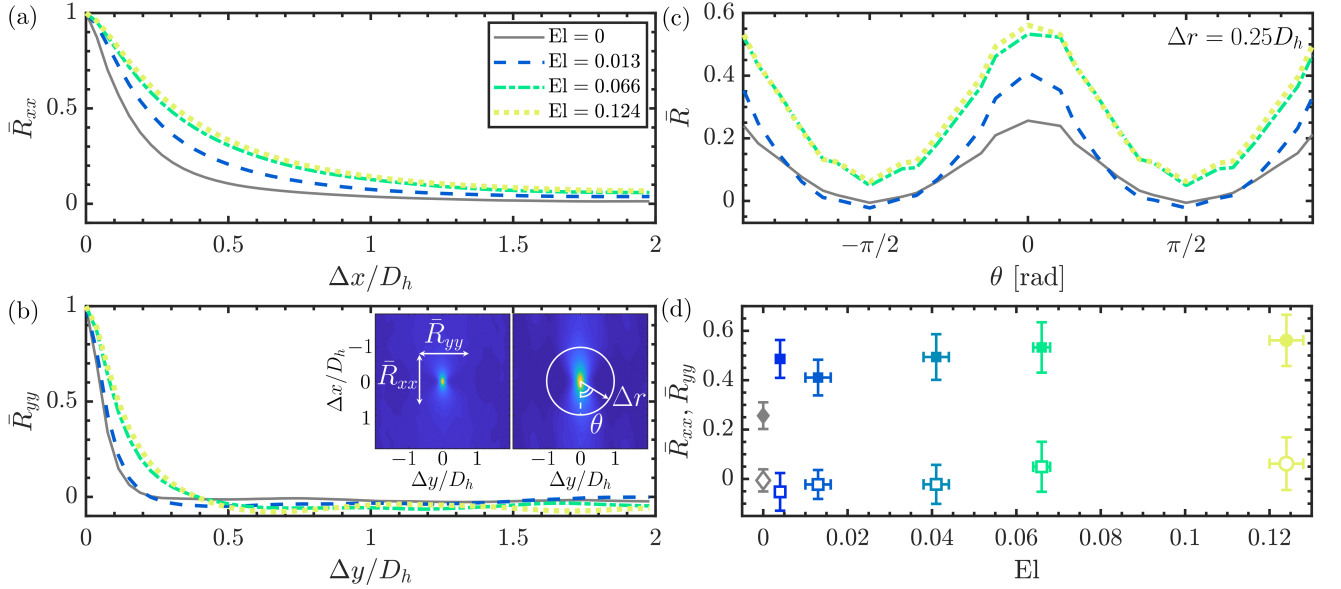


FIG. 9. (a) Decay in the streamwise (\bar{R}_{xx}) and (b) spanwise (\bar{R}_{yy}) autocovariance versus nondimensional streamwise ($\Delta x/D_h$) and spanwise ($\Delta y/D_h$) displacements for a Newtonian (El = 0) and for viscoelastic jets with El = 0.013, El = 0.066, and El = 0.124 at $Re = 400$. The left inset in (b) defines \bar{R}_{xx} and \bar{R}_{yy} , the right inset defines the polar coordinate system. (c) Autocovariance in a polar coordinate system ($R(\Delta r, \theta)$) for $\Delta r = 0.25D_h$. (d) Streamwise (filled symbols) and spanwise (hollow symbols) values of the autocovariance at $\Delta r = 0.25D_h$ as a function of elasticity number. The horizontal error bars denote the uncertainty in the elasticity number shown in Table I. The vertical error bars denote the standard deviations of \bar{R}_{xx} and \bar{R}_{yy} at $\Delta r = 0.25D_h$.

Finally, it is important to note that the global Weissenberg number defined based on the bulk flow properties does not characterize the dynamics of the viscoelastic jets in the fully turbulent region studied above. Here we define a local Weissenberg number based on turbulent properties as $Wi_T = \lambda u_{cl}^{RMS}/\ell_T$, where ℓ_T is the Taylor microscale. Adopting a frozen flow hypothesis [97], the Taylor microscale is defined as [98],

$$\ell_T = \left[-\frac{1}{2} \frac{d^2 \bar{R}_{xx}}{d(\Delta x/D_h)^2} \right]^{-1/2}, \quad (14)$$

such that the parabolic curve fitting of the computed \bar{R}_{xx} at $\Delta x/D_h = 0$ has the form,

$$p(\Delta x/D_h) = 1 - \frac{(\Delta x/D_h)^2}{(\ell_T/D_h)^2}, \quad (15)$$

and therefore $p(\ell_T) = 0$. Based on the parabola osculating \bar{R}_{xx} of the viscoelastic jet with $El = 0.013$, shown in Fig. 9(a), the Taylor microscale is $\ell_T = 0.183D_h = 1.33 \times 10^{-4}$ m, resulting in $Wi_T = 4.09$. This local Weissenberg number is greater than unity, which shows the relative importance of elasticity. This information together with the dimensionless parameters defined based on the bulk properties of the jets will allow for data-infused simulations of the viscoelastic planar jets.

D. Power spectral density of elasto-inertial turbulence

We calculate the PSD of the velocity fluctuations $E(f)$, also referred to as the turbulent kinetic energy spectrum, at a fixed Eulerian location $x = 40D_h$ and at the centerline of the jet from the fluctuating velocity time series $u_{cl}(t)$. For the Newtonian jet, the PSD exhibits a power-law decay with exponent -1.7 ± 0.2 in the inertial range, as shown in Fig. 10(a). The experimentally-determined power law exponent of -1.7 ± 0.2 is consistent with the well-known $-5/3$ power-law decay based on Kolmogorov's theory of Newtonian turbulence [30] and Taylor's frozen flow hypothesis [97], and expresses the balance between turbulent energy gain from the mean flow and the viscous dissipation of turbulent kinetic energy.

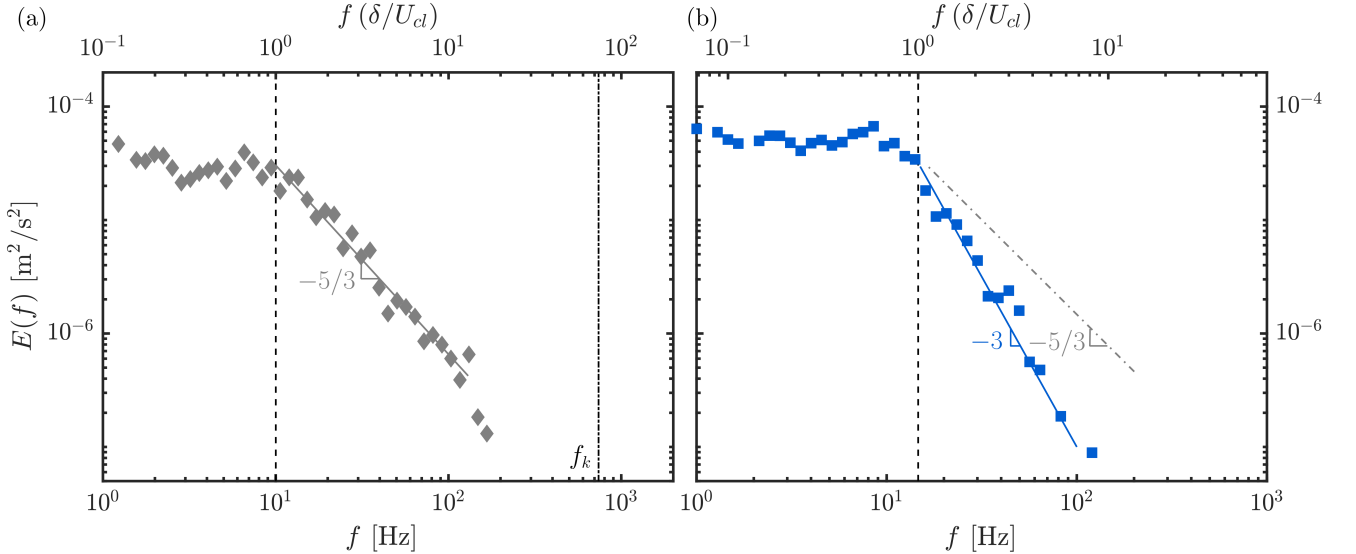


FIG. 10. Turbulent kinetic energy PSD for (a) a Newtonian jet (\blacklozenge) and (b) a viscoelastic jet (\blacksquare) with $El = 0.013$ at $Re = 400$, calculated at a streamwise distance $x = 40D_h$ from the nozzle and at the centerline of the turbulent jet. The bottom abscissa is the dimensional frequency, the top abscissa is the nondimensional frequency, normalized by δ/U_{cl} , where δ is the spreading of the jet and U_{cl} is the mean centerline velocity at $x = 40D_h$. The dimensionless frequency $f(\delta/U_{cl}) = 1$ denoting the onset of the inertial and elasto-inertial range of the spectrum is indicated by dashed lines. The Kolmogorov frequency f_k , at which the dominance of viscous effects terminates the inertial range of the spectrum, is indicated by the dashed-dotted line.

The turbulent kinetic energy spectrum evaluated at the centerline of the viscoelastic jet with $El = 0.013$ also exhibits self-similar behavior but with a different power-law decay characterised by an exponent of -2.9 ± 0.3 , as shown in Fig. 10(b). We have shown in our previous work [29] that the turbulent kinetic energy spectrum for viscoelastic jet flow contains a frequency range over which polymer chains sustain a persistent time-averaged rate of strain, $\langle \dot{\epsilon} \rangle \sim U_{cl}/\delta$, through repeated extension and relaxation [59]. Dimensional analysis then requires $E(k) \sim \langle \dot{\epsilon} \rangle^2 k^{-3}$ [27]. Considering the frozen flow hypothesis [97], $E(f) \sim f^{-3}$, where $f = (k/2\pi)U_{cl}$, in agreement with our data over a frequency range referred to as the elasto-inertial frequency range of the spectrum. We have also determined the turbulent kinetic energy spectrum for the same viscoelastic jet at $Re = 400$ and $x/D_h = 30, 20$ and at $Re = 200$ and $x/D_h = 40, 30, 20$; all of the turbulent kinetic energy spectra exhibit a power-law with average slope -2.8 ± 0.5 in the elasto-inertial range of frequencies.

The start of the inertial and elasto-inertial frequency range occurs approximately at the dimensionless frequency $f(\delta/U_{cl}) \sim 1$, as shown in Fig. 10(a) and (b), denoting the condition at which the frequency and the associated wavenumber correspond to the time and length scales of the largest eddies that can be generated in the flow. We note that for $f(\delta/U_{cl}) \lesssim 1$ (for the largest eddies and the largest turbulent fluctuations), the PSD in the viscoelastic spectrum is higher than in the Newtonian spectrum. At higher frequencies, however, the PSD of the viscoelastic jet rapidly falls below the Newtonian one due to its steeper power-law decay, as shown in the inset of Fig. 10(a). The higher power in EIT compared to Newtonian turbulence at smaller frequencies, or equivalently for larger eddies, considering the frozen flow hypothesis [97], is consistent with the schlieren observation of larger LCSs in the streamwise direction for EIT compared to Newtonian turbulence, as shown in Fig. 9. This is also an experimental evidence for the effect of polymer chains in altering the turbulent kinetic energy cascade by absorbing turbulence energy through their repeated extension and releasing it back to the flow through subsequent molecular relaxation [22, 25, 26, 34, 36, 37, 39, 99].

For Newtonian turbulence, dissipation becomes dominant at the Kolmogorov frequency where the smallest eddies are dissipated by viscosity. The Kolmogorov frequency, $f_k = 739$ Hz for our system is calculated in Appendix E, and is marked with vertical dashed line in Fig. 10(a) which shows that the measurement of the turbulent kinetic energy spectrum from LDV cannot resolve the entire inertial range of the spectrum. This range of the spectrum can, however, be accessed by calculating the spatial PSD of the intensity fluctuations in schlieren images. We show in Appendix F power-law decay rates for the spatial spectra (Fig. 19(a) and (b)) that are consistent with the TKE frequency spectra shown in Fig. 10(a) and (b) for Newtonian turbulence and EIT, respectively. In addition, the spatial PSD analysis extends the range of dimensionless frequency/wavenumber to two decades over which the $-5/3$ and -3 power-law decay rates are observed for Newtonian turbulence and EIT, respectively, as shown in Fig. 19(a) and (b). Finally, the wavenumber associated with Kolmogorov length scale can be resolved and the deviation from the $-5/3$ power-law is observed, as shown in Fig. 19(a).

EIT and its spectral properties have been areas of research interest and discovery. Early theoretical work on EIT has reported that below a critical Reynolds number, where the product of polymer relaxation time and principal Lyapunov exponent (*i.e.*, logarithmic rate of the divergence of two nearby Lagrangian trajectories) is smaller than unity, most polymers are in equilibrium and act as passive particles in the flow. Above this critical Reynolds number, however, the product of polymer relaxation time and principal Lyapunov exponent is larger than unity as a result of the polymers reaching an elongated state [31, 32] and contributing to the fluctuating flow by their energy storage and release. This contribution results in a power-law decay of the turbulent kinetic energy spectrum that is steeper than -3 [21]. Reference [27], however, discusses that this argument may not be conclusive as the physics changes when flow scales become smaller than the length of the polymer chains. The slope associated with the spectrum decay of EIT has also been studied in numerical simulations. While slopes as steep as $-14/3$ have been reported, without providing a physical or theoretical explanation [22–24], it has been shown through theoretical arguments that when the polymer relaxation time is not significantly larger than the Kolmogorov timescale [30], the turbulent kinetic energy spectrum decays with a slope of -3 [25, 26]. For this range of relaxation and Kolmogorov time scales, a fraction of the turbulent energy is transferred to and stored in the polymer chains, preventing it from being transferred to small scales of motion through the conventional Newtonian turbulent energy cascade [33]. Turbulent channel flow experiments [27, 28, 100], and experiments of submerged round jets [29] all report a power-law decay with slope -3 for the turbulent kinetic energy spectrum of EIT. Direct numerical simulations of viscoelastic jets [101], wakes [102], and Taylor-Couette flow [103] confirm slopes of -3 . In this work, we calculate the PSD for Newtonian turbulence and EIT using velocity fluctuations and intensity fluctuations of schlieren images that are a surrogate for concentration fluctuations (*cf.* Appendix F). Using these two approaches, we show a consistent -3 power-law decay for EIT over two decades of dimensionless frequency/wavenumber.

IV. CONCLUSIONS

Our experiments have revealed the emergence and evolution of inertio-elastic instabilities in submerged planar jets of dilute polymer solutions. We show that in jets characterized by small, non-zero elasticity a viscoelastic shear-layer instability emerges at the interface between the jet and the surrounding fluid that advances the transition to turbulence to lower Reynolds numbers and distances closer to the nozzle. This shear-layer instability evolves independently of a longer wavelength instability of the jet column. An increase in the elasticity number merges the sinuous shear-layer instability with the instability of the jet column. The two jet-column and shear-layer modes identified by our DMD analysis can be used to prescribe realistic initial perturbations in future simulations of turbulent viscoelastic jets.

At high Reynolds numbers, the Newtonian and viscoelastic jets transition to two distinctly different states identified as Newtonian turbulence and EIT, respectively. Elasto-inertial turbulence is characterized by universal features that are observed in our experiments for a wide range of elasticity numbers: The rate of spreading of jets in the EIT state is independent of elasticity number, but slower than that observed for a Newtonian jet, which indicates a smaller rate

of fluid entrainment for turbulent viscoelastic jets compared to Newtonian jets. Moreover, EIT exhibits Lagrangian coherent structures that are elongated in the streamwise direction with autocorrelations that are independent of elasticity number. These structures are consistent with the strong elasticity-driven decay in the spectrum of EIT, which results in a higher spectral energy for larger flow structures as well as f^{-3} power-law decay due to the contribution of the repeated stretching and relaxation of polymer chains to the turbulent energy cascade.

Our results motivate future numerical simulations of viscoelastic jets to probe the experimentally-observed universality of the EIT state for long chain flexible polymers over a wide range of elasticity numbers. Using data assimilation techniques, simulations that faithfully reproduce the measurements will also be able to provide predictive estimates of the full flow field in the jet, including the polymer conformation and elastic stresses.

ACKNOWLEDGMENTS

We are grateful to Dr. James W. Bales for his advice on building the schlieren imaging setup. We thank MSE Inc. for providing the miniLDV G5B sensor. This work was supported by the National Science Foundation (NSF) Grant No. CBET-2027870 to MIT and CBET-2027875 to JHU. We acknowledge the support of the Natural Sciences and Engineering Research Council of Canada (NSERC), funding reference number CGSD2-532512-2019. Cette recherche a été financée par le Conseil de recherches en sciences naturelles et en génie du Canada (CRSNG), numéro de référence CGSD2-532512-2019.

Appendix A: Calculation of power spectral density for LDV measurements

A time series measured with the LDV sensor is discrete and unevenly sampled over finite time, necessitating care in post-processing the data for spectral analysis. We employ the Lomb-Scargle periodogram method [70, 104, 105], assuming discrete values of $\tilde{U}_{cl}^i(x, t_i)$ are sampled at a fixed streamwise point x and at times t_i , where $i = 1, \dots, N$, such that there are N sampled data points. Defining the mean for the data,

$$U_{cl}(x) = \frac{1}{N} \sum_{i=1}^N \tilde{U}_{cl}^i(x, t_i), \quad (\text{A1})$$

the dimensional PSD with dimension $[\text{m}^2/\text{s}^2]$ is

$$E(f) = \frac{1}{N} \left[\frac{[\sum_{i=1}^N (\tilde{U}_{cl}^i(x, t_i) - U_{cl}(x)) \cos \omega(t_i - \tau)]^2}{\sum_{i=1}^N \cos^2 \omega(t_i - \tau)} + \frac{[\sum_{i=1}^N (\tilde{U}_{cl}^i(x, t_i) - U_{cl}(x)) \sin \omega(t_i - \tau)]^2}{\sum_{i=1}^N \sin^2 \omega(t_i - \tau)} \right], \quad (\text{A2})$$

where $\omega = 2\pi f$ and τ is evaluated from

$$\tan(2\omega\tau) = \frac{\sum_{i=1}^N \sin 2\omega t_i}{\sum_{i=1}^N \cos 2\omega t_i}. \quad (\text{A3})$$

The velocity time series, which is partly shown in Fig. 2(a) for a Newtonian turbulent jet at $\text{Re} = 400$, is segmented into one second blocks with 50% overlap. The PSD for each segment is calculated using the Lomb-Scargle periodogram method, and all segments are averaged (solid line in Fig. 2(b)). The frequencies are divided into logarithmically spaced bins and the mean power spectrum is averaged within each bin (hollow symbols shown in Fig. 2(b)).

Appendix B: Evolution equation for the radius of elastic filament in CaBER based on FENE-P model

We follow the derivation in [77] for the evolution equation of the filament radius over time based on the FENE-P model in the elasto-capillary regime. The dimensionless filament radius $\xi(t) = R(t)/R_0$ is given in implicit form by

$$-\frac{(b+3)^2}{b(b+2)}\tau = \left(\frac{1}{1+E_c(b+3)} - \frac{1}{1+\xi E_c(b+3)} \right) + 3 \ln \left(\frac{1+\xi E_c(b+3)}{1+E_c(b+3)} \right) + 4E_c \frac{(b+3)}{(b+2)} (\xi - 1), \quad (\text{B1})$$

where $b = 3L_{max}^2$, $\tau = t/\lambda_{\text{FENE-P}}$ is time nondimensionalized with the relaxation time parameter of the FENE-P model, E_c is the elasto-capillary number defined as $E_c = GR_0/\sigma$, the ratio between the elastic modulus of the suspension of dumbbells ($G \sim Nk_B T$) and the capillary pressure at the beginning of the elasto-capillary region σ/R_0 . The prediction of equation B1 best matches the experimental data using an empirical numerical factor of 6 such that $G = 6Nk_B T$. See [77] for additional discussion of the early time response of the filament before an elasto-capillary balance is fully established. Equation B1 simplifies to the exponential form expected for the Oldroyd-B constitutive model (eq. 11) in the limit where $b \rightarrow \infty$. Both models predict the evolution accurately in the elasto-capillary region, as shown in Fig. 3(b); however, in the region where the finite extensibility of the polymer chains becomes important (later times), the FENE-P model (solid black line) provides a more accurate description of the data compared to the Oldroyd-B model (dashed black line).

Appendix C: Flow visualization

Front-view and side-view snapshots of Newtonian and viscoelastic jets, with different elasticity numbers, are shown at different Reynolds numbers. Figures 11-13 show the impact of increasing elasticity number from $\text{El} = 0$ to $\text{El} = 0.124$ at fixed Reynolds numbers ranging from $\text{Re} = 100$ to $\text{Re} = 400$. Figures 14-16 show the impact of increasing Reynolds number from $\text{Re} = 100$ to $\text{Re} = 400$ at fixed elasticity numbers ranging from $\text{El} = 0$ to $\text{El} = 0.124$.

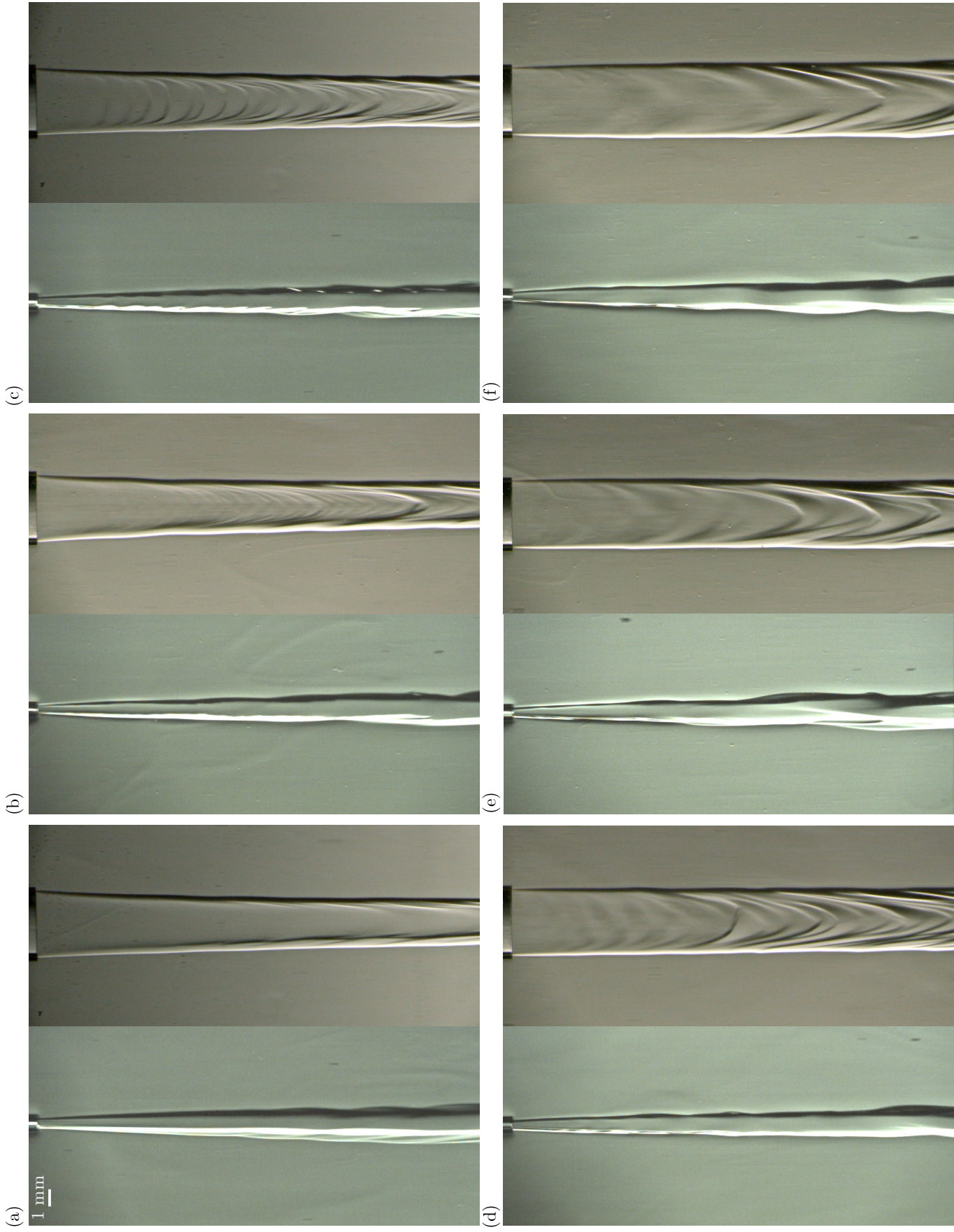


FIG. 11. Side-view and front-view schlieren snapshots of (a) the Newtonian jet ($El = 0$), and viscoelastic jets with elasticity numbers of (b) $El = 0.004$, (c) $El = 0.013$, (d) $El = 0.041$, (e) $El = 0.066$, and (f) $El = 0.124$ at $Re = 100$. The elasticity number and hence the Weissenberg number, $Wi \sim El \cdot Re/(1 - \beta)$, also increases from (a) to (f).

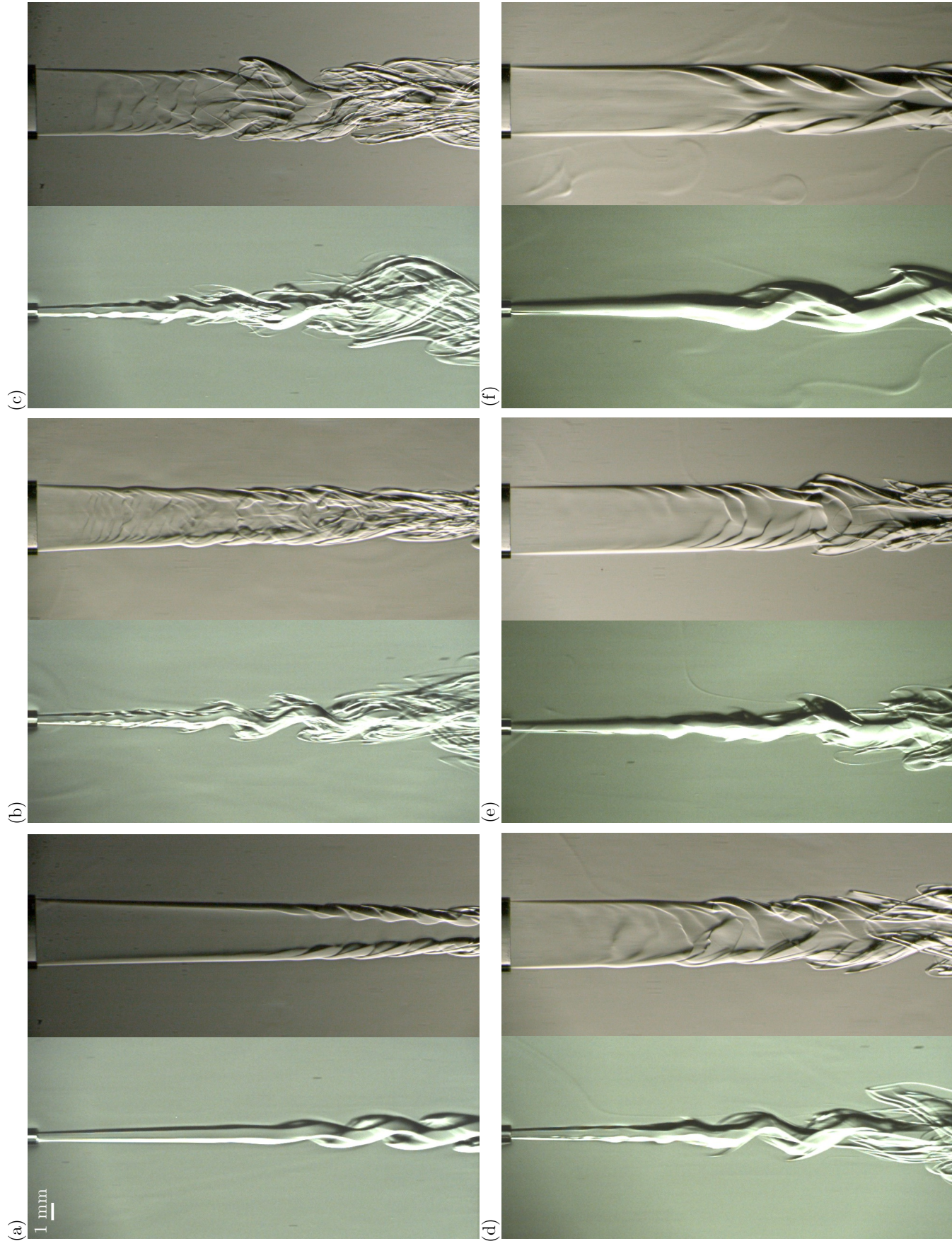


FIG. 12. Side-view and front-view schlieren snapshots of (a) the Newtonian jet ($El = 0$), (b) $El = 0.004$, (c) $El = 0.013$, (d) $El = 0.041$, (e) $El = 0.066$, and (f) $El = 0.124$ at $Re = 200$. The elasticity number and hence the Weissenberg number also increases from (a) to (f).

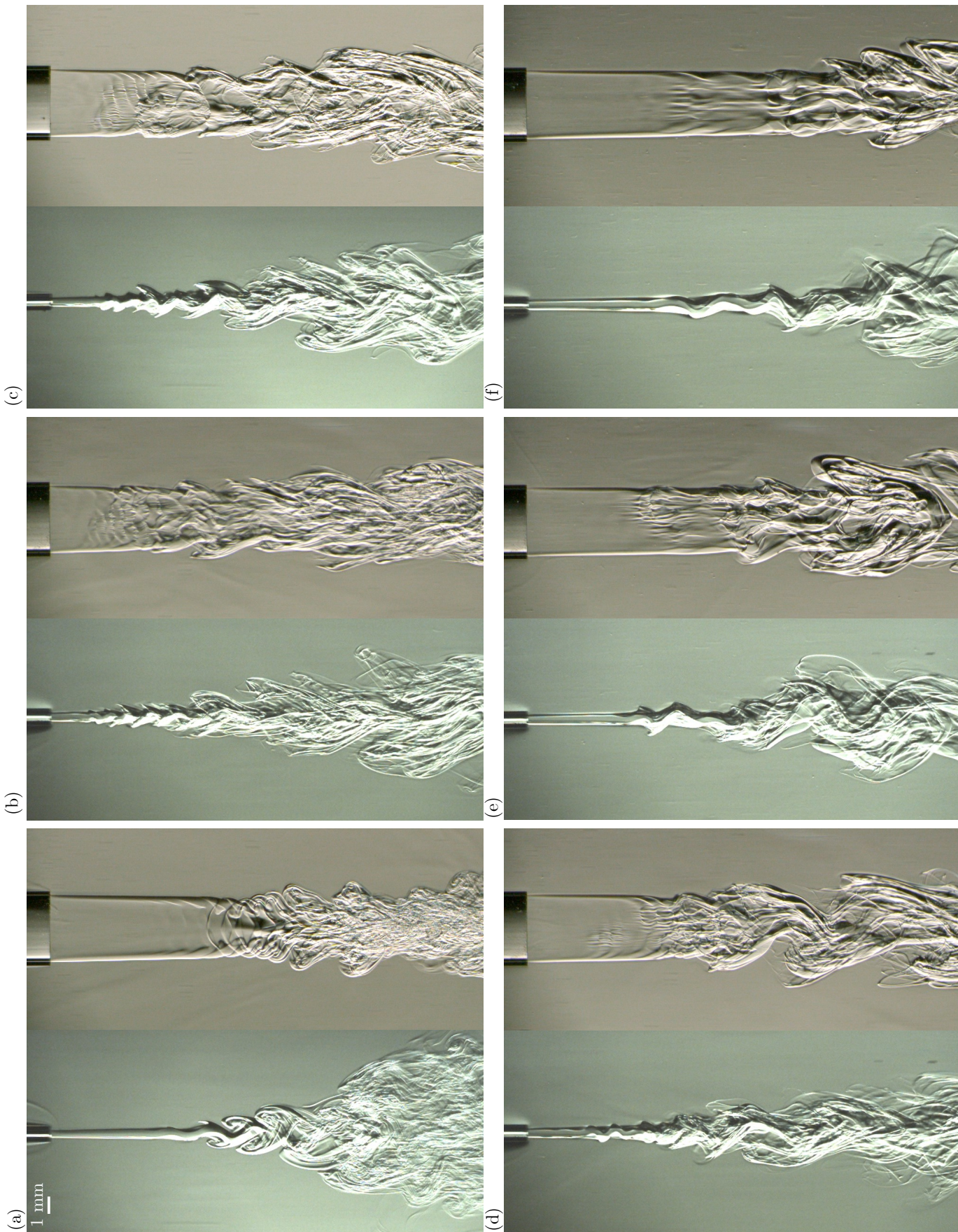


FIG. 13. Side-view and front-view schlieren snapshots of (a) the Newtonian jet ($El = 0$), (b) $El = 0.004$, (c) $El = 0.013$, (d) $El = 0.041$, (e) $El = 0.066$, and (f) $El = 0.124$ at $Re = 400$. The elasticity number and hence the Weissenberg number increases from (a) to (f).

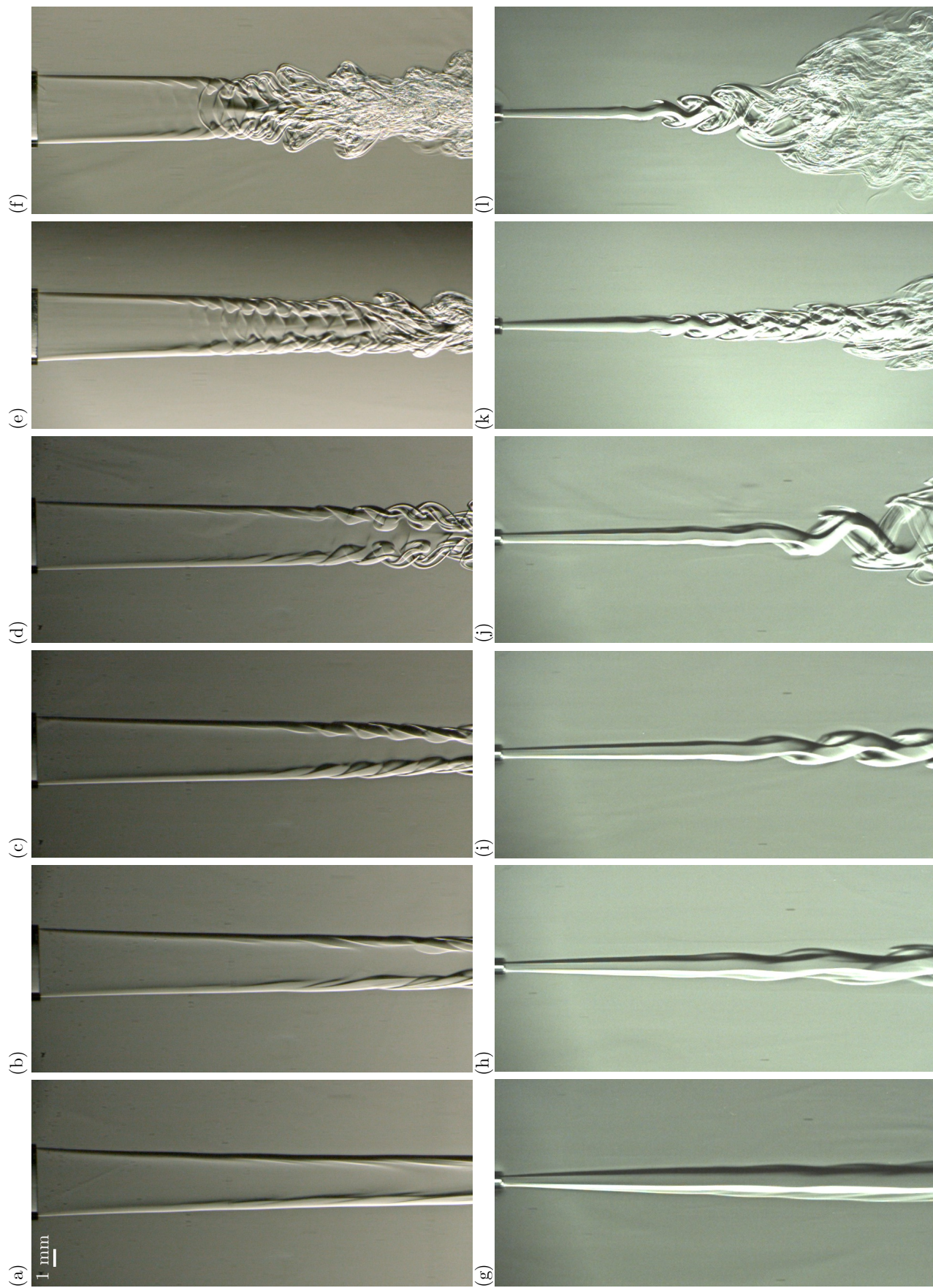


FIG. 14. Front-view schlieren snapshots of the Newtonian jet ($El = 0$) at (a) $Re = 100$, (b) $Re = 150$, (c) $Re = 200$, (d) $Re = 250$, (e) $Re = 300$, and (f) $Re = 400$. Side-view schlieren snapshots of the Newtonian jet ($El = 0$) at (g) $Re = 100$, (h) $Re = 150$, (i) $Re = 200$, (j) $Re = 250$, (k) $Re = 300$, and (l) $Re = 400$.

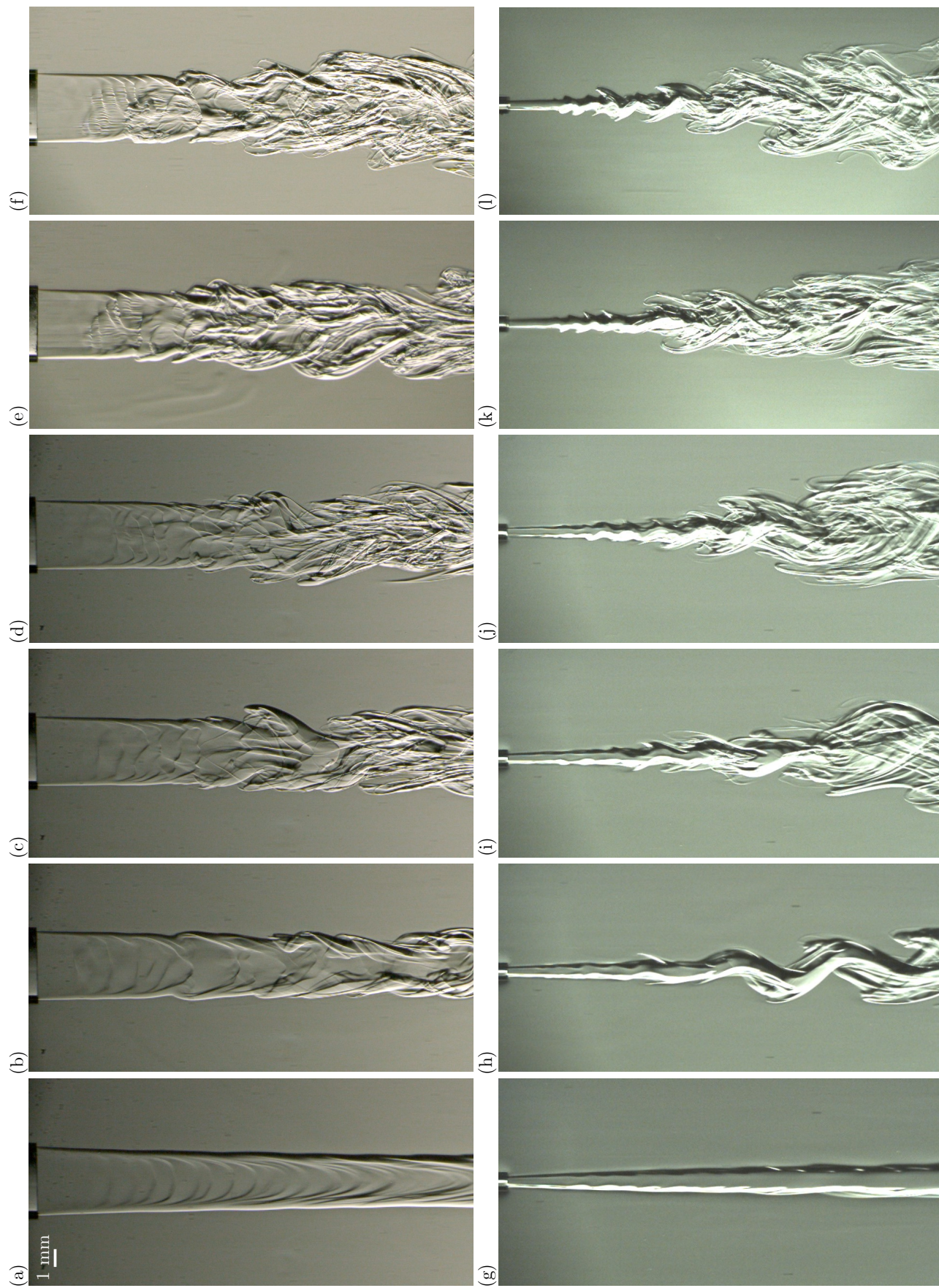


FIG. 15. Front-view schlieren snapshots of a weakly viscoelastic jet ($El = 0.013$) at (a) $Re = 100$, (b) $Re = 150$, (c) $Re = 200$, (d) $Re = 250$, (e) $Re = 300$, and (f) $Re = 400$. Side-view schlieren snapshots of the same jet ($El = 0.013$) at (g) $Re = 100$, (h) $Re = 150$, (i) $Re = 200$, (j) $Re = 250$, (k) $Re = 300$, and (l) $Re = 400$.

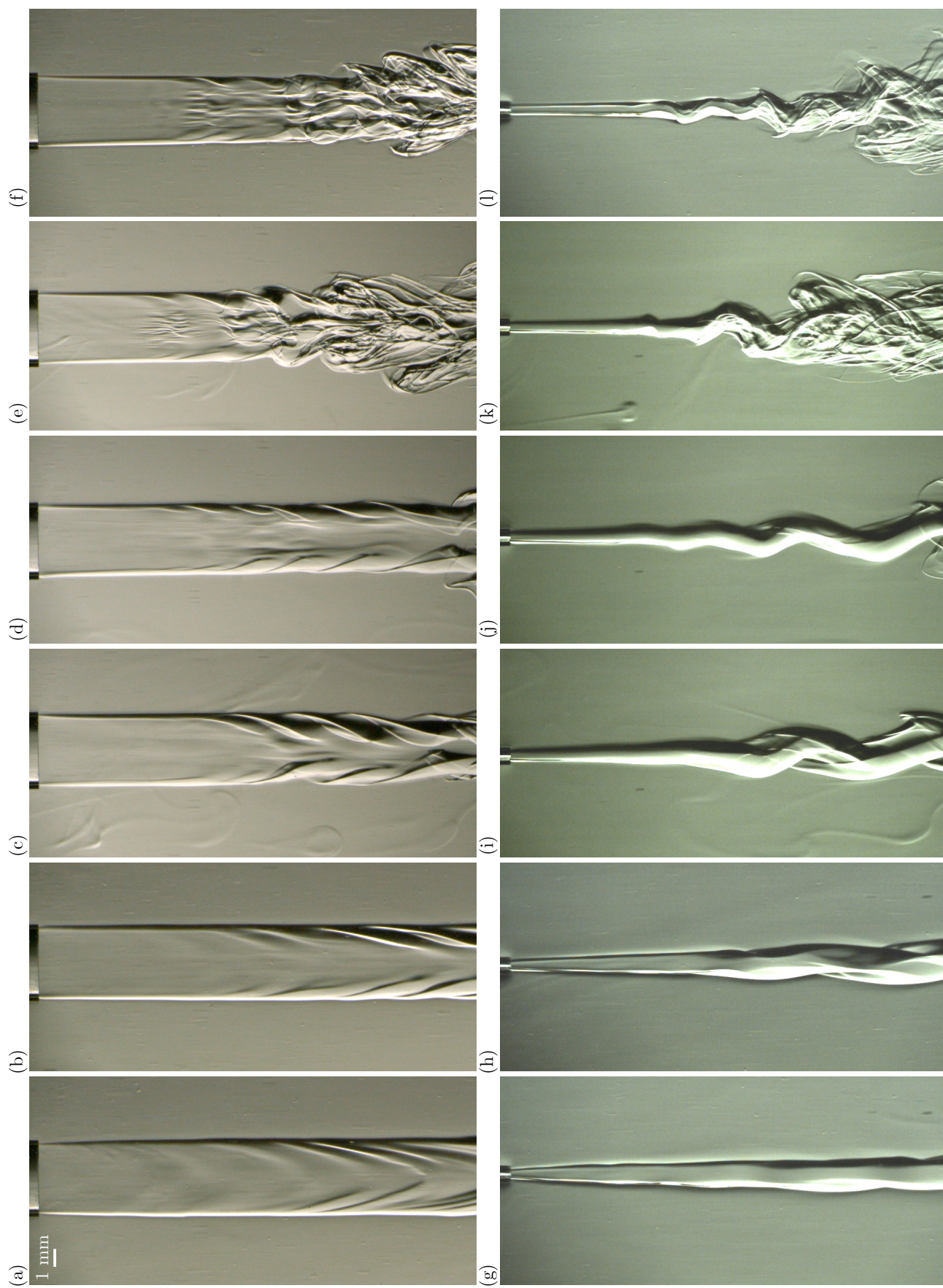


FIG. 16. Front-view schlieren snapshots of a more viscoelastic jet ($El = 0.124$) at (a) $Re = 100$, (b) $Re = 150$, (c) $Re = 200$, (d) $Re = 250$, (e) $Re = 300$, and (f) $Re = 400$. Side-view schlieren snapshots of the same jet ($El = 0.124$) at (g) $Re = 100$, (h) $Re = 150$, (i) $Re = 200$, (j) $Re = 250$, (k) $Re = 300$, and (l) $Re = 400$.

Appendix D: Dynamic mode decomposition (DMD)

The DMD results for a viscoelastic jet with $El = 0.013$ and at $Re = 100$ using different regions of interrogation are shown in Fig. 17. The regions of interrogation have the spanwise width $5D_h$ and varying streamwise lengths of $8D_h$, $10D_h$, and $12D_h$. Two wavenumber peaks at similar wavenumbers are observed for any choice of region of interrogation, confirming the robustness of the method used to identify the jet-column mode (marked by the black vertical lines) and the shear-layer mode (marked by the red vertical lines), as shown in Fig. 17(b)-(d). Note that smaller regions of interrogation restrict identification of low wavenumber modes, whereas larger regions of interrogation also potentially include the nonlinear evolution of the linear modes of the instability exhibited by the jet.

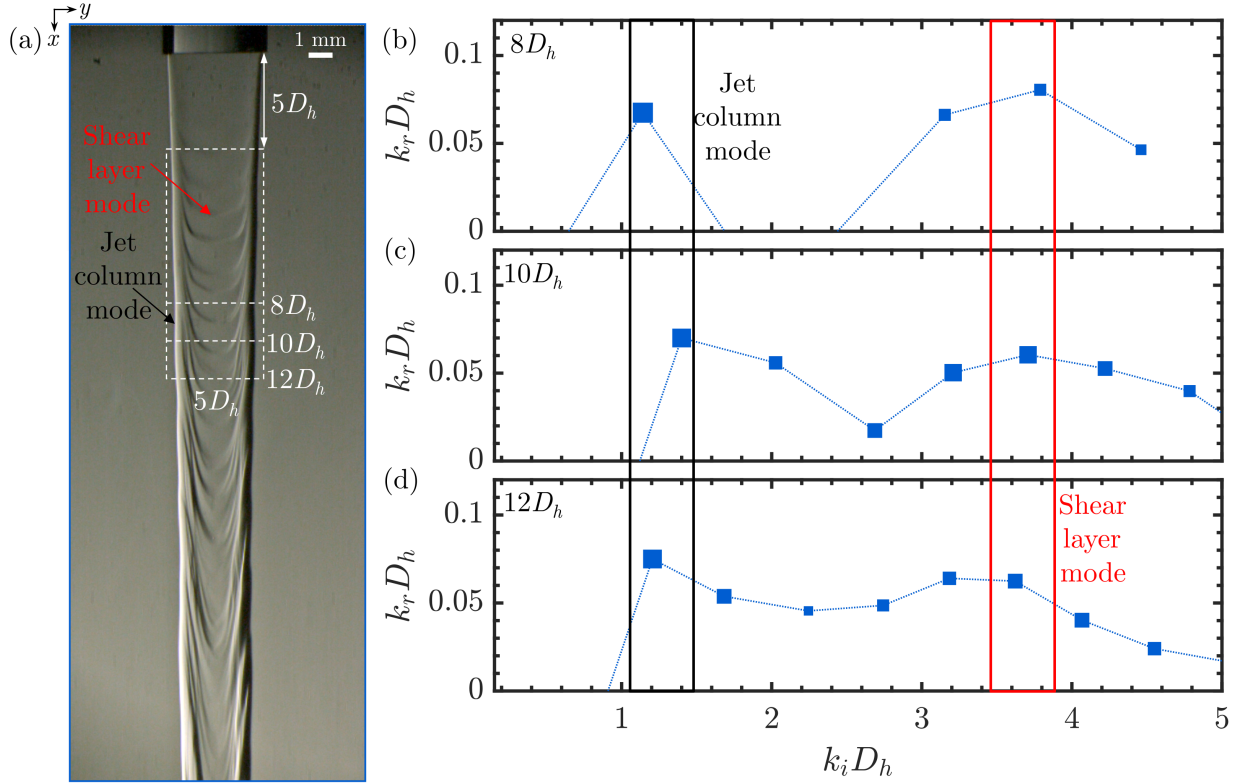


FIG. 17. (a) Front-view of the viscoelastic jet with $El = 0.013$ at $Re = 100$. The shear-layer and jet-column modes are identified with red and black arrows, respectively. The three investigated regions of interrogation are marked with dashed white lines. Wavenumber and growth rate of the jet for regions of interrogation with streamwise length (b) $8D_h$, (c) $10D_h$, and (d) $12D_h$. The abscissa and ordinate are nondimensionalized with the jet hydraulic diameter D_h . The size of the symbols denotes the relative magnitude of the amplitude of each mode $|b_j|$. The loci of the two peaks are marked with black and red bounding rectangles for the jet-column mode and shear-layer mode, respectively. The dashed lines are guides to the eye for identifying the local maxima in growth rate.

Similar to the spatial DMD discussion in Section III A, the analysis can be performed temporally to decompose the disturbances visualized by schlieren imaging into a set of orthogonal modes. The intensity signal $I(x, y, t)$ is expressed as a linear superposition of orthogonal modes $\phi(x, y)$, each having a complex amplitude b_j (where $|b_j|$ determines the relative importance of each mode), a frequency ω_i (which characterizes the periodicity of the mode in time, t) and a temporal growth rate ω_r (where $\omega_r > 0$ represents a temporally growing mode):

$$I(x, y, t) = \sum_{j=1}^{N_t} b_j \phi_j(x, y) \exp(\omega_r^j + i\omega_i^j)t, \quad (D1)$$

where $j = 1, 2, \dots, N_t$ and N_t is the total number of modes. We use the same approach discussed in Section III A to determine the retained number of modes for the temporal DMD analysis. Figure 18(b) and (c) compare the results of the temporal and spatial DMD analyses. As expected, all modes determined in the temporal case are stable, *i.e.*,

$\omega_r < 0$. The spatial analysis captures a number of downstream amplifying modes, $k_r > 0$, indicating that the jet is spatially unstable and that the instability is convective in nature.

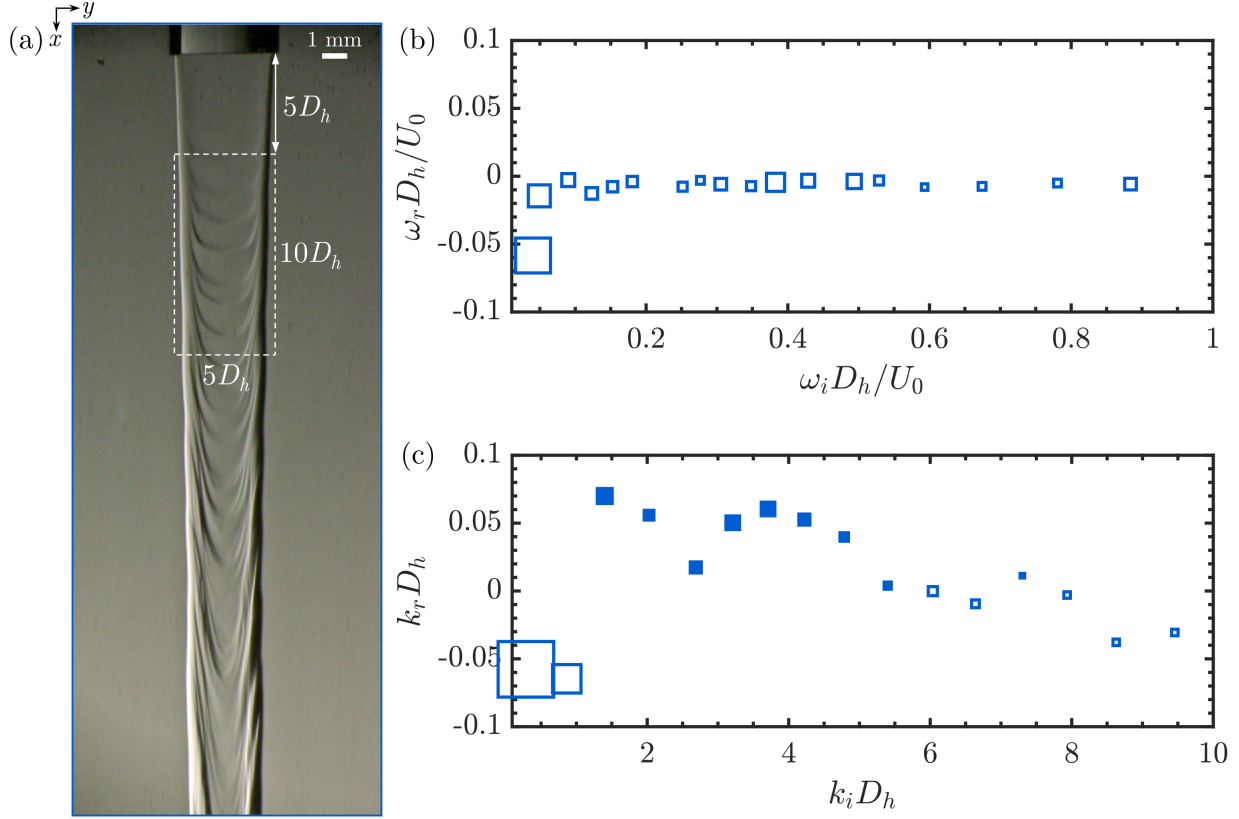


FIG. 18. (a) Front-view snapshot of a viscoelastic jet with $El = 0.013$ at $Re = 100$. (b) Frequency and temporal growth rate of the jet determined by temporal DMD analysis for the region of interrogation marked with white dashed lines in (a). The abscissa and ordinate are nondimensionalized with the jet hydraulic diameter D_h and the mean velocity at the exit of the nozzle U_0 . (c) Wavenumber and spatial growth rate of the jet determined by spatial DMD analysis. The abscissa and ordinate are nondimensionalized with the jet hydraulic diameter D_h . The size of the symbols denotes the relative magnitude of the amplitude of each mode $|b|$ with respect to the DC mode, *i.e.*, $\omega_i = 0$ and $k_i = 0$ for the temporal and spatial DMD analyses, respectively. Filled and hollow symbols denote unstable and stable modes, respectively.

Appendix E: Kolmogorov scale and the Taylor frozen field hypothesis

The production of turbulent kinetic energy scales as $\dot{W} \sim \overline{uw} (\partial U / \partial z)$ in the jet, where u and w are the streamwise and spanwise velocity fluctuations, U is the mean streamwise velocity and z is the spanwise direction. The largest eddies experience the mean shear, which is of order U_{cl}/δ , where $U_{cl}(x)$ is the mean centerline velocity and $\delta(x)$ the thickness of the jet at streamwise location x from the nozzle. Based on the maximum value reported for \overline{uw} in the spanwise direction for experimental studies with Reynolds numbers that are at least an order of magnitude higher than our studied Reynolds numbers [98, 106, 107], we estimate the order of magnitude for \overline{uw} to be $\sim 0.025U_{cl}^2$. This yields $\dot{W} \propto 0.025U_{cl}^2 (U_{cl}/\delta)$. An equilibrium argument, while admittedly crude, can provide a useful estimate of the turbulent kinetic energy dissipation rate, $\bar{\epsilon} \sim \dot{W}$. The associated Kolmogorov length scale is defined as $\ell_k = (\nu^3/\bar{\epsilon})^{1/4}$. For the Newtonian jet at streamwise distance $x = 40D_h$ from the nozzle, $U_{cl} = 0.1034$ m/s and $\delta = 0.0103$ m, which yields $\bar{\epsilon} = 2.7 \times 10^{-3}$ m²/s³ and $\ell_k = 1.4 \times 10^{-4}$ m. Because of the weak dependence of ℓ_k on $\bar{\epsilon}$, changes in the coefficient of scaling for \overline{uw} , *i.e.*, 0.025, does not change the estimate for ℓ_k appreciably. Using Taylor's frozen flow hypothesis [97], the Kolmogorov length scale calculated at the centerline of the Newtonian jet and at streamwise distance $x = 40D_h$ from the nozzle can be converted into a frequency scale, *i.e.*, $f_k = (\ell_k/U_{cl})^{-1} = 739$ Hz, as shown in Fig. 10(a).

Appendix F: Calculation of power spectral density for schlieren measurements

Schlieren images of the turbulent region of the jet provide spatial visualization of the changes in turbulent structures. The PSD of this signal can be calculated using FFT. We consider the spatial range $38D_h < x < 42D_h$, and the centerline of the jet. We denote the schlieren signal as $I^j(x_j, t)$ at fixed time t and Eulerian streamwise position x_j , where $j = 1, \dots, M$ and $M = 4D_h/\Delta = 104$ is the total number of pixels of size Δ . The PSD, $P(k)$, is normalized using the variance of the signal, $I^j(x_j, t)$. The results are time-averaged over 4000 frames, and the images are recorded at 4000 frames per second.

The intensity of the schlieren images represents the local concentration fluctuations as the jet mixes with the background fluid in the turbulent region [29]. At high Schmidt number, $Sc = \nu/D$ (where ν is the kinematic viscosity of the dilute polymer solution and D is the diffusivity of the individual polymer chains in the solvent), the PSD of concentration fluctuations exhibits an ‘inertio-convective range’ with the same power-law decay rate as the inertial range of the turbulent kinetic energy spectrum [108, 109]. A requirement for this similarity is a high Schmidt number, which is satisfied in our Newtonian and viscoelastic solutions ($\sim 10^3$ and $\sim 10^6$, respectively [29]).

Figures 19(a) and (b) show the time-averaged and normalized PSD of the intensity, $P(k)$, as a function of streamwise wavenumber, for the Newtonian and viscoelastic (El = 0.013) jets. The insets show a localized region of size $4D_h$ along the centerline of the jets, for which the power spectral densities are calculated. The power-law decays for the Newtonian and viscoelastic jets are the same as the respective frequency spectra of the turbulent kinetic energy (*cf.* Fig. 10(a) and (b)). To compare the scales spanned by the wavenumber spectra (Fig. 19(a) and (b)) and the frequency spectra (Fig. 10(a) and (b)), the upper abscissae are nondimensionalized with the jet spreading parameter δ (defined in Sec. III B) and δ/U_{cl} , respectively. The latter captures the energy cascade for large to medium size eddies, while the wavenumber spectra extend to small eddies. The Kolmogorov wavenumber is marked by a vertical dashed line in Fig. 19(a) at $k = 2\pi/\ell_k$, where ℓ_k is calculated in Appendix E. For the Newtonian jet, this scale is consistent with the end of the $-5/3$ power-law decay. The change in the spectral decay at this scale is less pronounced for the viscoelastic jet (Fig. 19(b)), at least for the range of wavenumbers accessible from the schlieren images.

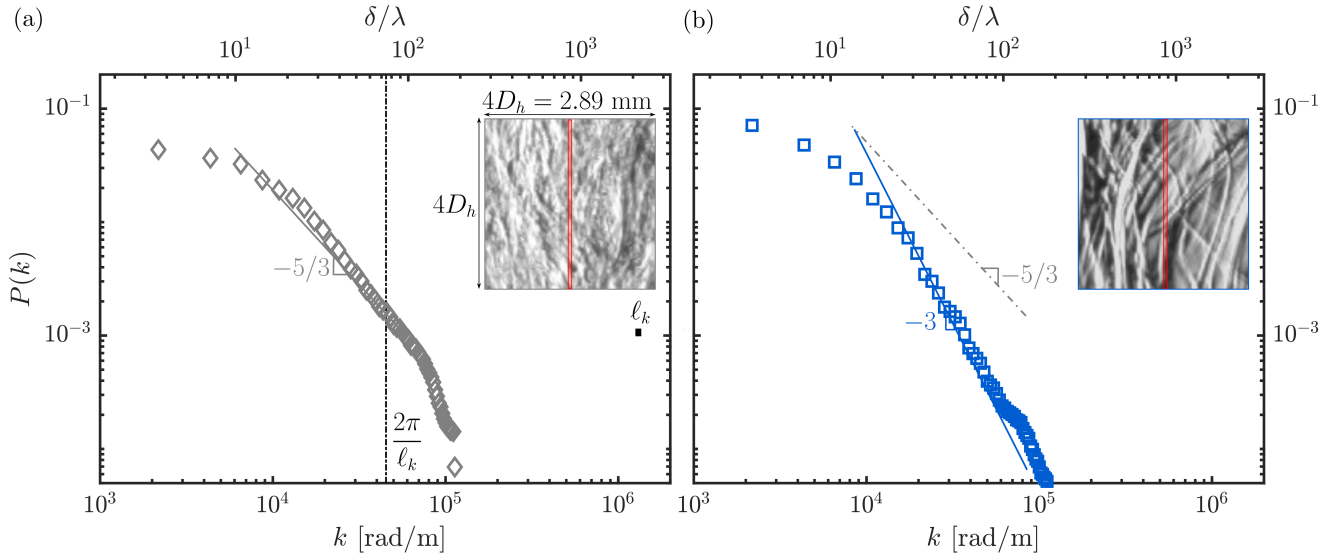


FIG. 19. PSD of concentration fluctuations for (a) the Newtonian jet (\blacklozenge) and (b) the viscoelastic jet (\blacksquare) with El = 0.013 at Re = 400, calculated over a streamwise range $38D_h < x < 42D_h$ from the nozzle and along the centerline of the turbulent jet. The upper axes are nondimensionalized with δ and $\lambda = k/2\pi$. The insets of (a) and (b) show snapshots from schlieren videos used to calculate the PSD for the Newtonian and viscoelastic jets. The red rectangles mark the spatial signal used for each jet at the centerline of the jet. The Kolmogorov length scale (ℓ_k) for the Newtonian jet, compared to the size of the spatial domain, is shown by the black line below the inset. The vertical dashed line in (a) marks the wavenumber associated with the Kolmogorov length scale.

-
- [1] E. D. Burger, W. R. Munk, and H. A. Wahl, Flow increase in the trans Alaska pipeline through use of a polymeric drag-reducing additive, *J. Petrol. Technol.* **34**, 377 (1982).
 - [2] M. Perlin and S. Ceccio, *Mitigation of hydrodynamic resistance: Methods to reduce hydrodynamic drag* (World Scientific, 2014).
 - [3] W. Bouchenafa, B. Dewals, A. Lefevre, and E. Mignot, Water soluble polymers as a means to increase flow capacity: Field experiment of drag reduction by polymer additives in an irrigation canal, *J. Hydraul. Eng.* **147**, 05021003 (2021).
 - [4] B. A. Toms, Some observations on the flow of linear polymer solutions through straight tubes at large Reynolds numbers, *Proc. of Int. Cong. On Rheology* **2**, 135 (1948).
 - [5] K. Mysels, Early experiences with viscous drag reduction, in *AIChE Chemical Engineering Progress Symposium Series III*, Vol. 67 (1971) pp. 45–49.
 - [6] E. S. Winkel, G. F. Oweis, S. A. Vanapalli, D. R. Dowling, M. Perlin, M. J. Solomon, and S. L. Ceccio, High-Reynolds-number turbulent boundary layer friction drag reduction from wall-injected polymer solutions, *J. Fluid Mech.* **621**, 259 (2009).
 - [7] P. S. Virk, E. W. Merrill, H. S. Mickley, K. A. Smith, and E. L. Mollo-Christensen, The Toms phenomenon: turbulent pipe flow of dilute polymer solutions, *J. Fluid Mech.* **30**, 305 (1967).
 - [8] P. S. Virk, Drag reduction fundamentals, *AIChE J.* **21**, 625 (1975).
 - [9] L. Zhu and L. Xi, Nonasymptotic elastoinertial turbulence for asymptotic drag reduction, *Phys. Rev. Fluids* **6**, 014601 (2021).
 - [10] D. Samanta, Y. Dubief, M. Holzner, C. Schäfer, A. N. Morozov, C. Wagner, and B. Hof, Elasto-inertial turbulence, *Proc. Natl. Acad. Sci. USA* **110**, 10557 (2013).
 - [11] G. H. Choueiri, J. M. Lopez, A. Varshney, S. Sankar, and B. Hof, Experimental observation of the origin and structure of elastoinertial turbulence, *Proc. Natl. Acad. Sci. USA* **118**, e2102350118 (2021).
 - [12] G. H. Choueiri, J. M. Lopez, and B. Hof, Exceeding the asymptotic limit of polymer drag reduction, *Phys. Rev. Lett.* **120**, 124501 (2018).
 - [13] J. M. Lopez, G. H. Choueiri, and B. Hof, Dynamics of viscoelastic pipe flow at low Reynolds numbers in the maximum drag reduction limit, *J. Fluid Mech.* **874**, 699 (2019).
 - [14] R. B. Bird, R. C. Armstrong, and O. Hassager, *Dynamics of Polymeric Liquids. Vol. 1: Fluid mechanics* (Wiley, 1987).
 - [15] J. Azaiez and G. M. Homsy, Linear stability of free shear flow of viscoelastic liquids, *J. Fluid Mech.* **268**, 37 (1994).
 - [16] P. K. Ray and T. A. Zaki, Absolute instability in viscoelastic mixing layers, *Phys. Fluids* **26**, 014103 (2014).
 - [17] J. Azaiez and G. M. Homsy, Numerical simulation of non-Newtonian free shear flows at high Reynolds numbers, *J. Non-Newton. Fluid* **52**, 333 (1994).
 - [18] S. Kumar and G. M. Homsy, Direct numerical simulation of hydrodynamic instabilities in two-and three-dimensional viscoelastic free shear layers, *J. Non-Newton. Fluid* **83**, 249 (1999).
 - [19] J. M. Rallison and E. J. Hinch, Instability of a high-speed submerged elastic jet, *J. Fluid Mech.* **288**, 311 (1995).
 - [20] P. K. Ray and T. A. Zaki, Absolute/convective instability of planar viscoelastic jets, *Phys. Fluids* **27**, 014110 (2015).
 - [21] A. Fouxon and V. Lebedev, Spectra of turbulence in dilute polymer solutions, *Phys. Fluids* **15**, 2060 (2003).
 - [22] Y. Dubief, V. E. Terrapon, and J. Soria, On the mechanism of elasto-inertial turbulence, *Phys. Fluids* **25**, 110817 (2013).
 - [23] L. Thais, G. Mompean, and T. Gatski, Spectral analysis of turbulent viscoelastic and newtonian channel flows, *J. Non-Newton. Fluid* **200**, 165 (2013).
 - [24] T. Watanabe and T. Gotoh, Hybrid Eulerian–Lagrangian simulations for polymer–turbulence interactions, *J. Fluid Mech.* **717**, 535 (2013).
 - [25] P. Valente, C. Da Silva, and F. Pinho, The effect of viscoelasticity on the turbulent kinetic energy cascade, *J. Fluid Mech.* **760**, 39 (2014).
 - [26] P. C. Valente, C. B. da Silva, and F. T. Pinho, Energy spectra in elasto-inertial turbulence, *Phys. Fluids* **28**, 075108 (2016).
 - [27] R. Vonlanthen and P. A. Monkewitz, Grid turbulence in dilute polymer solutions: PEO in water, *J. Fluid Mech.* **730**, 76 (2013).
 - [28] M. Warholic, H. Massah, and T. Hanratty, Influence of drag-reducing polymers on turbulence: effects of Reynolds number, concentration and mixing, *Exp. Fluids* **27**, 461 (1999).
 - [29] S. Yamani, B. Keshavarz, Y. Raj, T. A. Zaki, G. H. McKinley, and I. Bischofberger, Spectral universality of elastoinertial turbulence, *Phys. Rev. Lett.* **127**, 074501 (2021).
 - [30] A. N. Kolmogorov, The local structure of isotropic turbulence in an incompressible viscous fluid, in *Dokl. Akad. Nauk SSSR*, Vol. 30 (1941) pp. 301–305.
 - [31] E. Balkovsky, A. Fouxon, and V. Lebedev, Turbulent dynamics of polymer solutions, *Phys. Rev. Lett.* **84**, 4765 (2000).
 - [32] E. Balkovsky, A. Fouxon, and V. Lebedev, Turbulence of polymer solutions, *Phys. Rev. E* **64**, 056301 (2001).
 - [33] H. Abreu, F. T. Pinho, and C. B. da Silva, Turbulent entrainment in viscoelastic fluids, *J. Fluid Mech.* **934** (2022).
 - [34] L. Xi and M. D. Graham, Active and hibernating turbulence in minimal channel flow of Newtonian and polymeric fluids, *Phys. Rev. Lett.* **104**, 218301 (2010).
 - [35] L. Xi and M. D. Graham, Turbulent drag reduction and multistage transitions in viscoelastic minimal flow units, *J. Fluid Mech.* **647**, 421 (2010).
 - [36] M. D. Graham, Drag reduction and the dynamics of turbulence in simple and complex fluids, *Phys. Fluids* **26**, 625 (2014).

- [37] A. S. Pereira, G. Mompean, L. Thais, E. J. Soares, and R. L. Thompson, Active and hibernating turbulence in drag-reducing plane Couette flows, *Phys. Rev. Fluids* **2**, 084605 (2017).
- [38] S.-N. Wang, A. Shekar, and M. D. Graham, Spatiotemporal dynamics of viscoelastic turbulence in transitional channel flow, *J. Non-Newton. Fluid* **244**, 104 (2017).
- [39] Y. Dubief, C. M. White, V. E. Terrapon, E. S. Shaqfeh, P. Moin, and S. K. Lele, On the coherent drag-reducing and turbulence-enhancing behaviour of polymers in wall flows, *J. Fluid Mech.* **514**, 271 (2004).
- [40] W. Li and M. D. Graham, Polymer induced drag reduction in exact coherent structures of plane Poiseuille flow, *Phys. Fluids* **19**, 083101 (2007).
- [41] P. A. Stone, A. Roy, R. G. Larson, F. Waleffe, and M. D. Graham, Polymer drag reduction in exact coherent structures of plane shear flow, *Phys. Fluids* **16**, 3470 (2004).
- [42] A. Agarwal, L. Brandt, and T. A. Zaki, Linear and nonlinear evolution of a localized disturbance in polymeric channel flow, *J. Fluid Mech.* **760**, 278 (2014).
- [43] S. Sid, V. Terrapon, and Y. Dubief, Two-dimensional dynamics of elasto-inertial turbulence and its role in polymer drag reduction, *Phys. Rev. Fluids* **3**, 011301 (2018).
- [44] S. J. Lee and T. A. Zaki, Simulations of natural transition in viscoelastic channel flow, *J. Fluid Mech.* **820**, 232 (2017).
- [45] A. Shekar, R. M. McMullen, S.-N. Wang, B. J. McKeon, and M. D. Graham, Critical-layer structures and mechanisms in elastoinertial turbulence, *Phys. Rev. Lett.* **122**, 124503 (2019).
- [46] A. Shekar, R. M. McMullen, B. J. McKeon, and M. D. Graham, Self-sustained elastoinertial Tollmien-Schlichting waves, *J. Fluid Mech.* **897** (2020).
- [47] A. Shekar, R. M. McMullen, B. J. McKeon, and M. D. Graham, Tollmien-schlichting route to elastoinertial turbulence in channel flow, *Phys. Rev. Fluids* **6**, 093301 (2021).
- [48] P. Garg, I. Chaudhary, M. Khalid, V. Shankar, and G. Subramanian, Viscoelastic pipe flow is linearly unstable, *Phys. Rev. Lett.* **121**, 024502 (2018).
- [49] J. Page, Y. Dubief, and R. R. Kerswell, Exact traveling wave solutions in viscoelastic channel flow, *Phys. Rev. Lett.* **125**, 154501 (2020).
- [50] G. Buza, J. Page, and R. R. Kerswell, Weakly nonlinear analysis of the viscoelastic instability in channel flow for finite and vanishing reynolds numbers, *J. Fluid Mech.* **940** (2022).
- [51] Y. Dubief, J. Page, R. R. Kerswell, V. E. Terrapon, and V. Steinberg, First coherent structure in elasto-inertial turbulence, *Phys. Rev. Fluids* **7**, 073301 (2022).
- [52] A. Gyr, Effects of polymer additives on the large scale structure of a two-dimensional submerged jet, *Appl. Sci. Res.* **56**, 13 (1996).
- [53] M. Hibberd, M. Kwade, and R. Scharf, Influence of drag reducing additives on the structure of turbulence in a mixing layer, in *Progress and Trends in Rheology* (Springer, 1982) pp. 228–232.
- [54] D. White, Velocity measurements in axisymmetric jets of dilute polymer solutions, *J. Fluid Mech.* **28**, 195 (1967).
- [55] Z. Shul'Man, N. Pokryvailo, N. Kovalevskaya, and V. Kulebyakin, Measurement of the turbulent flow structure of submerged jets of polymer solutions, *J. Eng. Phys.* **25**, 1475 (1973).
- [56] N. S. Berman and H. Tan, Two-component laser Doppler velocimeter studies of submerged jets of dilute polymer solutions, *AIChE J.* **31**, 208 (1985).
- [57] N. S. Berman, Dispersion measurements in a polymer solution turbulent submerged jet, in *AIP Conf. Proc.*, Vol. 137 (American Institute of Physics, 1986) pp. 129–133.
- [58] M. C. Guimarães, N. Pimentel, F. T. Pinho, and C. B. da Silva, Direct numerical simulations of turbulent viscoelastic jets, *J. Fluid Mech.* **899** (2020).
- [59] E. J. Hinch, Mechanical models of dilute polymer solutions in strong flows, *Phys. Fluids* **20**, S22 (1977).
- [60] See the Supplemental Material at [URL_will_be_inserted_by_publisher](#), which includes eight movies. movies 1-6 compare schlieren videos of a Newtonian jet and a viscoelastic jet at different Reynolds numbers. movies 7 and 8 show the impact of increasing elasticity number for a low and a high Reynolds number.
- [61] G. S. Settles, *Schlieren and Shadowgraph Techniques* (Springer, 2001).
- [62] W. M. bin Mat Yunus and A. bin Abdul Rahman, Refractive index of solutions at high concentrations, *Appl. Optics* **27**, 3341 (1988).
- [63] M. Rubinstein and R. H. Colby, *Polymer Physics* (Oxford University Press, 2003).
- [64] J. Brandrup, E. H. Immergut, E. A. Grulke, A. Abe, and D. R. Bloch, *Polymer handbook*, Vol. 7 (Wiley, 1989).
- [65] H. C. Price, J. Mattsson, and B. J. Murray, Sucrose diffusion in aqueous solution, *Phys. Chem. Chem. Phys.* **18**, 19207 (2016).
- [66] M. Warholic, *Modification of turbulent channel flow by passive and additive devices*, Ph.D. thesis, University of Illinois at Urbana-Champaign (1997).
- [67] M. Niederschulte, R. Adrian, and T. Hanratty, Measurements of turbulent flow in a channel at low Reynolds numbers, *Exp. Fluids* **9**, 222 (1990).
- [68] A. Günther, D. Papavassiliou, M. Warholic, and T. Hanratty, Turbulent flow in a channel at a low Reynolds number, *Exp. Fluids* **25**, 503 (1998).
- [69] R. Adrian and C. Yao, Power spectra of fluid velocities measured by laser Doppler velocimetry, *Exp. Fluids* **5**, 17 (1986).
- [70] W. H. Press, S. A. Teukolsky, B. P. Flannery, and W. T. Vetterling, *Numerical recipes in Fortran 77: the art of scientific computing, volume 1* (Cambridge university press, 1992).
- [71] R. Pamies, J. G. H. Cifre, M. d. C. L. Martínez, and J. G. de la Torre, Determination of intrinsic viscosities of macromolecules and nanoparticles. Comparison of single-point and dilution procedures, *Colloid Polym. Sci.* **286**, 1223 (2008).

- [72] A. Rajappan and G. H. McKinley, Epidermal biopolysaccharides from plant seeds enable biodegradable turbulent drag reduction, *Sci. Rep.* **9**, 1 (2019).
- [73] V. Tirtaatmadja, G. H. McKinley, and J. J. Cooper-White, Drop formation and breakup of low viscosity elastic fluids: Effects of molecular weight and concentration, *Phys. Fluids* **18**, 043101 (2006).
- [74] A. M. Shetty and M. J. Solomon, Aggregation in dilute solutions of high molar mass poly (ethylene) oxide and its effect on polymer turbulent drag reduction, *Polymer* **50**, 261 (2009).
- [75] M. S. Oliveira, R. Yeh, and G. H. McKinley, Iterated stretching, extensional rheology and formation of beads-on-a-string structures in polymer solutions, *J. Non-Newton. Fluid* **137**, 137 (2006).
- [76] C. Clasen, J. Eggers, M. A. Fontelos, J. Li, and G. H. McKinley, The beads-on-string structure of viscoelastic threads, *J. Fluid Mech.* **556**, 283 (2006).
- [77] C. Wagner, L. Bourouiba, and G. H. McKinley, An analytic solution for capillary thinning and breakup of FENE-P fluids, *J. Non-Newton. Fluid* **218**, 53 (2015).
- [78] T. A. Zaki and M. Wang, From limited observations to the state of turbulence: Fundamental difficulties of flow reconstruction, *Physical Review Fluids* **6**, 100501 (2021), publisher: American Physical Society.
- [79] Q. Wang, Y. Hasegawa, and T. A. Zaki, Spatial reconstruction of steady scalar sources from remote measurements in turbulent flow, *J. Fluid Mech.* **870**, 316 (2019).
- [80] Y. Du, M. Wang, and T. A. Zaki, State estimation in minimal turbulent channel flow: A comparative study of 4DVar and PINN, *International Journal of Heat and Fluid Flow* **99**, 10.1016/j.ijheatfluidflow.2022.109073 (2023).
- [81] N. Burshtein, K. Zografos, A. Q. Shen, R. J. Poole, and S. J. Haward, Inertioelastic flow instability at a stagnation point, *Phys. Rev. X* **7**, 041039 (2017).
- [82] K. Devanand and J. C. Selser, Asymptotic behavior and long-range interactions in aqueous solutions of poly (ethylene oxide), *Macromolecules* **24**, 5943 (1991).
- [83] P. J. Schmid, Dynamic mode decomposition of numerical and experimental data, *J. Fluid Mech.* **656**, 5 (2010).
- [84] J. N. Kutz, S. L. Brunton, B. W. Brunton, and J. L. Proctor, *Dynamic mode decomposition: data-driven modeling of complex systems* (SIAM, 2016).
- [85] F. O. Thomas and K. M. K. Prakash, An experimental investigation of the natural transition of an untuned planar jet, *Phys. Fluids A-Fluid* **3**, 90 (1991).
- [86] N. Otsu, A threshold selection method from gray-level histograms, *IEEE transactions on systems, man, and cybernetics* **9**, 62 (1979).
- [87] D.-Y. Huang and C.-H. Wang, Optimal multi-level thresholding using a two-stage Otsu optimization approach, *Pattern Recogn. Lett.* **30**, 275 (2009).
- [88] K. P. Nolan and T. A. Zaki, Conditional sampling of transitional boundary layers in pressure gradients, *J. Fluid Mech.* **728**, 306 (2013).
- [89] P. L. Miller and P. E. Dimotakis, Measurements of scalar power spectra in high Schmidt number turbulent jets, *J. Fluid Mech.* **308**, 129 (1996).
- [90] N. E. Kotsovinos, A note on the spreading rate and virtual origin of a plane turbulent jet, *J. Fluid Mech.* **77**, 305 (1976).
- [91] P. R. Suresh, K. Srinivasan, T. Sundararajan, and S. K. Das, Reynolds number dependence of plane jet development in the transitional regime, *Phys. Fluids* **20**, 044105 (2008).
- [92] S. C. Shadden, Lagrangian coherent structures, in *Transport and Mixing in Laminar Flows* (Wiley, 2011) pp. 59–89.
- [93] G. Haller, D. Karrasch, and F. Kogelbauer, Material barriers to diffusive and stochastic transport, *P. Natl. Acad. Sci. USA* **115**, 9074 (2018).
- [94] H. W. Emmons, The laminar-turbulent transition in a boundary layer-Part I, *J. Aeronaut. Sci.* **18**, 490 (1951).
- [95] B. Cantwell, D. Coles, and P. Dimotakis, Structure and entrainment in the plane of symmetry of a turbulent spot, *J. Fluid Mech.* **87**, 641 (1978).
- [96] O. Marxen and T. A. Zaki, Turbulence in intermittent transitional boundary layers and in turbulence spots, *Journal of Fluid Mechanics* **860**, 350–383 (2019).
- [97] G. I. Taylor, The spectrum of turbulence, *Proc. R. Soc. Lon. Ser-A* **164**, 476 (1938).
- [98] S. B. Pope, *Turbulent flows* (Cambridge university press, 2000).
- [99] J. Page and T. A. Zaki, Streak evolution in viscoelastic Couette flow, *J. Fluid Mech.* **742**, 520 (2014).
- [100] R. S. Mitishita, G. J. Elfring, and I. A. Frigaard, Statistics and spectral analysis of turbulent duct flows with flexible and rigid polymer solutions, *J. Non-Newton. Fluid Mech.* , 104952 (2022).
- [101] G. Soligo and M. E. Rosti, Non-newtonian turbulent jets at low-reynolds number, arXiv preprint arXiv:2206.05450 (2022).
- [102] M. C. Guimarães, F. T. Pinho, and C. B. da Silva, Turbulent planar wakes of viscoelastic fluids analysed by direct numerical simulations, *J. Fluid Mech.* **946** (2022).
- [103] J. M. Lopez, Vortex merging and splitting events in viscoelastic Taylor–Couette flow, *J. Fluid Mech.* **946** (2022).
- [104] N. R. Lomb, Least-squares frequency analysis of unequally spaced data, *Astrophys. Space Sci.* **39**, 447 (1976).
- [105] J. D. Scargle, Studies in astronomical time series analysis. II-Statistical aspects of spectral analysis of unevenly spaced data, *Astrophys. J.* **263**, 835 (1982).
- [106] B. Viggiano, T. Dib, N. Ali, L. G. Mastin, R. B. Cal, and S. A. Solovitz, Turbulence, entrainment and low-order description of a transitional variable-density jet, *J. Fluid Mech.* **836**, 1009 (2018).
- [107] S. Stanley, S. Sarkar, and J. Mellado, A study of the flow-field evolution and mixing in a planar turbulent jet using direct numerical simulation, *J. Fluid Mech.* **450**, 377 (2002).
- [108] A. M. Oboukhov, Structure of the temperature field in turbulent flows, *Isv. Geogr. Geophys. Ser.* **13**, 58 (1949).
- [109] S. Corrsin, On the spectrum of isotropic temperature fluctuations in an isotropic turbulence, *J. Appl. Phys.* **22**, 469

(1951).